Flow and Temperature Patterns in an Inductively Coupled Plasma Reactor: Experimental Measurements and CFD Simulations

Sangeeta B. Punjabi
Electrical Engineering Dept., V.J.T.I, Matunga, Mumbai 400019, India

Dept. of Physics, University of Mumbai, Kalina 400098, India

Sunil N. Sahasrabudhe, S. Ghorui, A. K. Das
Laser and Plasma Technology Division, BARC, Mumbai 400085, India

Narendra K. Joshi
Dept. of Nuclear Science and Technology, Modi University of Science and Technology, Lakshamnagarh (Sikar)−332311, India

Dushyant C. Kothari
Dept. of Physics, University of Mumbai, Kalina 400098, India

Arijit A. Ganguli
Dept. of Chemical Engineering, Institute of Chemical Technology, Matunga, Mumbai 400019, India

Jyeshtharaj B. Joshi
Dept. of Chemical Engineering, Institute of Chemical Technology, Matunga, Mumbai 400019, India

Homi Bhabha National Institute, Anushaktinagar, Mumbai 400094, India

DOI 10.1002/aic.14547

Measurements of temperature patterns in an inductively coupled plasma (ICP) have been carried out experimentally. Plasma torch was operated at different RF powers in the range of 3–14 kW at near atmospheric pressure and over a wide range of sheath gas flow rate (3–25 lpm). Measurements were made at five different axial positions in ICP torch. The chordal intensities were converted into a radial intensity profile by Abel Inversion technique. Typical radial temperature profile shows an off-axis temperature peak, which shifts toward the wall as the power increases. Temperatures in the range of 6000–14,000 K were recorded by this method. The temperature profiles in the plasma reactor were simulated using computational fluid dynamics (CFD). A good agreement was found between the CFD predictions of the flow and temperature pattern with those published in the literature as well as the temperature profiles measured in the present work. © 2014 American Institute of Chemical Engineers *AIChE J*, 60: 3647–3664, 2014

Keywords: plasma reactor, flow pattern, computational fluid dynamics, spectroscopy, temperature, imaging, fluid mechanics

Introduction

The plasma reactors have potentially wide applications in the production of high purity materials, surface treatment, surface coatings, chemical synthesis, and chemical processing.[1–4] Table 1 gives the examples of practical importance where plasma reactors are useful.[5–14] From Table 1, it can be seen that the plasma reactors can be advantageously used for the synthesis of several useful molecules, nanoparticles, catalysts, and composites.

The plasma reactors are of different types: (1) corona discharge (pulsed or silent discharge) plasma reactors (2) dielectric barrier discharge plasma reactors (3) inductively coupled plasma (ICP) reactors (4) thermal plasma jet reactors, and so forth. The present work is concerned with the radio-frequency inductively coupled plasma (RF-ICP) reactors. The understanding of basic phenomena involved in these systems and the ability to control the conditions of discharge are vital for the successful implementation of RF-ICP in practice. Plasma is regarded as a multifunctional fluid, because it has a high energy density, chemical reactivity, and variable transport properties. However, control of plasma by application of a magnetic field is difficult due to the instability of plasma in a RF induction discharge. One of the

---

Correspondence concerning this article should be addressed to S. N. Sahasrabudhe at sns@barc.gov.in or J. B. Joshi at jbjoshi@gmail.com

Table 1. Plasma Reactors: Examples of Industrial Importance

Sr. No	Author	Application	Remarks
1	Liao et al.[5]	Destruction of perflourocarbons using inductively coupled plasma (ICP) reactor	Nearly 100% destruction (or abatement) efficiency was obtained for C_2F_6, C_2F_4, and CF_3. The effect of power input, residence time, type of additive gas going into the reactor, and Argon dilution have been observed
2	Guddeti et al.[6]	Depolymerization of polypropylene using ICP	This work deals with decomposition of polypropylene into propylene and other useful chemicals. The effect of parameters which have been tested are: Power input, Sheath gas flow rate variation, central gas flow variation, powder feed rate, and quench gas flow rate
3	Mohai et al.[7]	Zinc and ferrous removal and recovery of metals	The reduction rate depends on feed rate of powders. Gradient cooling is required for separation of metals. Valuable products can be obtained.
4	Bretagnol et al.[8]	Surface modification of polyethylene powder by nitrogen and ammonia and low pressure plasma in fluidized bed reactor	Combination of fluidized bed and plasma for manufacture of low density polyethylene powders (LDPE). The plasma gas considered was nitrogen for one case and ammonia for the other. Increase in hydrophilic character of surface treated LDPE powder was seen.
5	Ye et al.[9]	Numerical modeling of ICP under thermal and nonequilibrium conditions	A numerical model has been presented, which takes care of thermal and chemical nonequilibrium. The chemical and thermal nonequilibrium occurring in the reactor can be reduced by adding hydrogen to argon plasma.
6	Abanades et al.[10]	Gas cleaning	Removal of NH_3, NO, and NO_x with concentration 10–40 ppm in air is performed. High removal efficiency of 93% and 0.6 s residence time is obtained
7	Jia and Gitzhofer[11]	Nanoparticle sizing in a Thermal plasma Synthesis reactor	ICP reactor has been used for the production of CeO_2 nanopowders. Results indicated that size distribution of synthesized nanopowders is locally monomodal with particle sizes as small as 4 nm.
8	Blanchard et al.[12]	Fischer–Tropsch synthesis in a slurry reactor using nanocarbide catalyst	The authors have prepared a new catalyst by plasma technology using ICP reactor for its application in Fischer–Tropsch synthesis
9	Hody et al.[13]	Production of silicon carbide nanoparticles in a fluidized bed reactor	The paper deals with coating composites by treatment in an ICP reactor. The characteristics of the composite material depended on interaction between the filler and the matrix. The main advantage of plasma technology is that it provides environmental and technical advantages as compared to wet processes
10	Pristavita et al.[14]	Carbon black produced in a plasma reactor	The paper deals with production of Carbon Black (CB) nanopowder by plasma decomposition of methane. In the conventional geometry, particle size of CB particles is much higher than that desired for many applications. Another problem is the formation of other volatile compounds. The geometry of ICP was changed and crystalline CB particles were synthesized and the desired particle size and shape were obtained.

methods for controlling of plasma is to use fluid dynamic techniques such as injection of a cold secondary gas and mixing of different kinds of gases.

Previous work

In this section, we present some of the most important experimental and mathematical (computational fluid dynamics [CFD]) studies for understanding the characteristics (temperature, velocity, magnetic field, and energy distributions) in an RF-ICP torch in a chronological manner. We then present the motivation for the present work.

Experimental investigations

The temperature and the flow patterns and the electron number density of ICP depend on various operating parameters like the input power, frequency, plasma, and sheath gas flow rates and the coil position (Kelliget and El-Kaddah[15]). Kornblum and de Galan[16] measured the temperature of various atomic and ionic species in a low power ICP at three different heights above the induction coil. Barnes and Scheicher[17] have reported velocity and temperature profiles near the induction coil region of an ICP used for spectrochemical analysis. Radial profiles of temperature, electron density, and electrical conductivity at different heights above the coil were studied in a 10.3 MHz ICP (Joshi et al.[18]). Hughes and Wooding[19] have measured radial profiles of temperature, electron density, and conductivity in a RF plasma torch with six turn water cooled coil and working at 5.1 MHz. However, there is a paucity of data on axial temperature profiles and the effect of sheath gas flow rate on the radial and axial temperature profiles in the coil region.

Theoretical investigations

Prediction of flow and temperature characteristics of RF-ICP using numerical models have been performed by various researchers.[20–25] In most cases, two-dimensional (2-D) axisymmetric models have been used. Earlier researchers[20,21] have used laminar Navier–Stokes equations for flow and temperature while 1-D models have been used for solving the electromagnetic (EM) field. Modeling the EM is the

Table 2. Literature Review of Mathematical Modeling of ICP

Authors	Geometry	Software Used	Findings	Assumptions	Conclusions	Limitations
Mostaghimiet al.[20]	2-D axisymmetric geometry. Flow and temperature in both r and z directions while electric and magnetic equations only in the r-direction	In-house code	1, 2, 6	2, 3, 4, 5, 10	1, 2, 3, 4	3
Boulos[21]	2-D axisymmetric geometry flow and temperature in both r and z directions while electric and magnetic equations only in the r-direction	In-house code	1	1, 2, 3, 4, 5, 6, 7, 8, 9, 10	8	3
Mostaghimi and Boulos[22]	2-D axisymmetric with both electric and magnetic 2-D equations	In-house code	3	2, 3, 4, 5, 10	6	1, 2
Xue et al.[24]	2-D axisymmetric geometry All equations are solved in both r and z directions	FLUENT	5	3, 4, 5, 10	7	
Bernardi et al.[25]	2-D axisymmetric geometry All equations are solved in both directions	FLUENT	4, 5, 6	3, 4, 5, 10	5	1, 4

Findings: **(1)** Flow and temperature fields in a ICP system have been estimated by solving governing equations of flow and temperature in 2-D while the electric and magnetic governing equations being solved in only 1-D. **(2)** Variation of various parameters which affect the flow and temperature characteristics of plasma were studied and important insights have been explained. **(3)** A new CFD model for solving 2-D equations of magnetic and electric field has been proposed for coupling with the flow and energy governing equations. 4**(4)** A new technique for solving 2-D equations of magnetic and electric field has been proposed for coupling with the flow and energy governing equations. 5**(5)** Different boundary conditions using an extended wall boundary condition has been studied. **(6)** 3-D effects for wall boundary conditions were studied.

Assumptions: **(1)** Flow field is affected by local plasma temperature changes. **(2)** Axially symmetric system of coordinates with 1-D electrical and magnetic fields and 2-D flow and temperature fields. **(3)** Steady state, incompressible, laminar flow. **(4)** Negligible viscous dissipation. **(5)** Local thermodynamic equilibrium. **(6)** Volumetric power input due to ohmic heating. **(7)** Radiation heat losses can be treated as a volumetric heat sink. **(8)** The plasma is optically thin. **(9)** Thermal conductivity includes in addition to molecular transport, effects such as energy transfer by thermal diffusion, ionization and recombination and equilibrium radiation for which the optical path is small compared to the size of the plasma. **(10)** Negligible displacement currents.

Conclusions: **(1)** Central gas injection has a negligible effect on the overall energy balance of the torch. **(2)** Keeping power constant, increasing total flow rate (summation of flow rates of central gas, sheath gas and plasma gas) results in effective heat transfer from plasma to the sheath gas so that lower water flow rates for external cooling can be used. **(3)** Keeping gas flow constant if power is increased, heat loss due to radiation is increased. The effective power being utilized for plasma formation is reduced due to these heat losses. **(4)** When the gas used for formation of plasma is changed from argon to nitrogen, the characteristics remain the same except the temperature level is substantially lower while velocities are higher. **(5)** Comparison of simulation results with literature data showed good agreement. **(6)** The results of 2-D governing equations for electric and magnetic field were better than the 1-D models and some better insights were also obtained. **(7)** The extended wall boundary condition gives similar results to the earlier technique but reduces CPU time drastically. **(8)** First 1-D model developed gave vital insights about the flow and temperature fields.

Limitations: **(1)** No parametric study was done for studying the effect on flow and temperature fields. **(2)** Boundary conditions were not properly specified. **(3)** The electric and magnetic governing equations being solved in only 1-D while temperature and flow equations were solved in 2-D. **(4)** No experimental validation of the model has been done

most critical task in the simulation of induction plasma torches. Hence, 2-D models have been proposed for solving EM. However, the boundary conditions used to implement these models introduce a strong nonlinear coupling between the boundary values of the vector potential and the current density distribution induced in the plasma. Hence, different formulations for solving EM equations have been proposed. A summary of the previous work on the numerical models used by various authors, their findings, assumptions, and limitations have been presented in Table 2.

A detailed parametric study was undertaken by Mostaghimi et al.[20] to understand the effect of various parameters on flow and temperature fields in an RF-ICP using CFD simulations. The frequency for all the cases were maintained 3 MHz. A 2-D axisymmetric domain was selected. Though the mass, momentum, energy, and concentration equations were 2-D, the equations for electric and magnetic fields were 1-D. Flow was assumed to be laminar and hence there was no need for any turbulence model. The parameters studied included the flow rates of central injection (carrier) gas (Q_1), plasma gas (Q_2), sheath gas (Q_3), input power (P), and the type of plasma gas (argon and nitrogen). The authors considered four cases: (1)The type of plasma gas was argon and the power was 3 kW; total gas flow rate ($Q_0 = Q_1 + Q_2 + Q_3$) was 20 lpm; plasma gas flow rate (Q_2) was 3 lpm; and central gas flow rate varied from 1 to 7 lpm. To maintain total gas flow rate constant the sheath gas flow rate (Q_3) was adjusted as per the variation of Q_1. In Case (2), the type of gas was nitrogen and the power was 10 kW; and Q_2 was varied from 0 to 5 lpm, while Q_1 was maintained at 3 lpm and $Q_3$was kept constant to maintain the total flow rate Q_0 at 20 lpm. In case (3), the type of gas was again argon and the power was kept constant at 5 kW, while the total gas flow rate was varied from 20 to 50 lpm. Q_1 was kept zero, while the plasma gas flow rate (Q_2) was varied from 3 to 7.5 lpm. For each variation, Q_3 was again adjusted to keep Q_0 constant. In Case (4), the power was varied from 3 to 10 kW and all the gas flow rates, that is, Q_1, Q_2, and Q_3, were kept constant with values of 1, 3, and 16 lpm, respectively.

The authors have made several useful observations. For Case (1), variation in central gas flow rate showed strong recirculations for low flow rates (1 lpm $< Q_1 <$ 3 lpm) while the recirculations diminished for high flow rates (3 lpm $< Q_1 <$ 7 lpm). The temperature profiles showed that the axial temperatures were practically the same as that of the inlet temperature for the whole length of the coil. This observation was made, however, only for $Q_1 = 7$ lpm. The radial profiles showed a decrease in temperature at the center of the torch with an increase in Q_1. However, the central gas flow rate change had no effect on the energy distribution and almost 60% of the energy was lost by radiation and conduction in the range of parameters investigated. For with nitrogen plasma [Case (2)], the temperature levels were lowered by 20% than those of argon plasma, while the velocities were found to be about 1.5 times higher than those of argon plasma. The effect of central gas flow rate was similar to that obtained by argon plasma. In Case (3), it was observed that, an increase in the total gas flow rate (which correspondingly increases the sheath gas flow rate), decreased temperatures close to the wall. As the total gas flow rate was increased the conduction losses to the wall decreased, while the radiation losses remained practically constant. Hence, the enthalpy of the exit gas was found to increase linearly with an increase in the total gas flow rate. In Case (4), however, as the power was increased the wall losses were found to decrease while the radiation losses increased. Thus, for a given gas flow rate, an increase in the total power of the torch resulted in substantial increase in the fraction of input power lost by radiation accompanied by a slight drop in conduction heat losses.

In a detailed review on RF-ICP, Boulos[21] has explained the characterization of ICP reactors (namely temperature distribution, velocity distribution, electric and magnetic field and concentration distributions) in the discharge region. The above characteristics reported by various researchers have been analyzed and presented in the review. The experimental measurements and the mathematical models used by different investigators to understand the flow and temperature fields have been comprehensively presented. Important conclusions were drawn from the investigations of Mostaghimi et al.[20] The influence of EM forces on flow field was noted to be substantial and was responsible for the formation of two circulation eddies in the discharge region with the downstream eddy being swept away with an increase in the plasma gas flow rate. The effect of confined and free plasma discharge on the characteristics in the induction zone had been performed by CFD simulations by various investigators. The results were presented in the review and showed that the flow fields in both the cases were similar in the induction zone while the temperature fields were slightly different. The effect of central gas flow rate (1–7 lpm) was also studied using CFD simulations. The simulations were performed for constant plasma gas flow rate and constant total gas flow rate. The increase in central gas flow rate resulted in cooling of the entrance region and high temperature region moved toward the wall. Though, the review presented the state of the art results of both the experimental measurements and the CFD simulations, the comparison of experimental data with simulations was not presented. Further, laminar model was chosen for the CFD simulations while the basis for the selection was not explained.

Mostaghimi and Boulos[22] extended the CFD model presented by Boulos.[21] Here, a 2-D model for the estimation of the EM field was presented instead of an 1-D model. Using the model, the authors have reported detailed flow, temperature, and EM field patterns and profiles. The profiles were compared with the earlier model (Mostaghimi et al.[20]). Temperature profiles were similar to the ones obtained by the 1-D model while velocity profiles were slightly different. The authors have pointed out that, in the 2-D case, the backflow of gas has been observed by Mostaghimi et al.[20] for lower flow rates and on the upstream end of the coil. This was due to the effect of the EM field on the gas causing reduction in backflow. When the axial magnetic field distribution along the centerline of the torch was plotted it was observed that the distribution was not symmetric with respect to the coil but was found to drop monotonously from one end of the coil to the other. Further, the radial magnetic field intensities were much lower than the axial field intensities, which explained why 2-D model was important. An excellent description of the interplay of the magnetic field, the temperature, and velocity fields was presented. The model was, however, not validated with the experimental data on the flow and temperature profiles available in the published literature.

Nishiyama et al.[23] extended the model of Mostaghimi and Boulos[22] to include the existence of turbulence in real practice of ICPs. Therefore, for the first time, they included the turbulence model in the CFD simulations. The torch dimensions were slightly different than those used by Mostaghimi and Boulos.[22] The values of Q_1, Q_2, and Q_3 were 20, 10, and 100 lpm, respectively. The grid size considered was low (62×36) and fourth-order Runge–kutta method was used to solve EM field equations. The authors investigated the effect of EM field, input power, position of secondary gas injection, and swirling on the characteristics of the plasma torch. The authors observed that, for different power inputs, the gas temperature increases toward the wall and attain a maximum at a region of maximum energy accumulation. With an increase in the power, a slight increase in the gas temperature was noted. In the case of axial velocity, it was observed to be maximum in the central region. The authors, further, observed that, in Case (a), the ratio of μ_t/μ was 0.5 upto 75% of the axial distance (along the centerline) from entry of the gas. For the rest 25% (till the exit), the ratio became almost 1. For Cases (b) and (c) in the wall region (50% of radial distance from the wall), the ratio μ_t/μ was found to be 0.5 (for 50% of the axial distance from entry of the gas) and becomes higher than one as one goes toward the center of the torch. An important conclusion was that the turbulent kinetic energy is high in Case (a) due to active mixing in the central region. For Case (c), the turbulent kinetic energy was found to be higher near the wall. In all investigations presented above, the domain considered was 2-D axisymmetric with radius R_C and height H_T.

Xue et al.[24] used a domain with radius twice of R_C such that the boundary of the domain was not confined around the coil but also away from the coil. However, only the vector potential equations were solved in the extended domain, while all the other equations were solved inside the confinement tube. By this modification, the calculation domain was divided into five zones: Zone I represented the plasma flow; zone II, the coil; Zone III, the plasma confinement tube; Zone IV, quartz tube to separate the central and sheath gas; and Zone V, the extended domain except the coil region. The boundary conditions at the wall were simplified as compared with those formulated by Mostaghimi and Boulos.[22] Due to the distance, the real and imaginary parts of the vector potential could now be set to zero at the wall of extended domain. Hence, Xue et al.[24] named this model as the extended field (EF) EM model. The authors compared the results of the EF model with the standard two-dimensional (ST) model and found that the predictions were better than the ST model (5% deviation). The main advantage of the EF model was the ability to predict the effects of coil geometry on the EM field. Further, the computational time was also reduced.

Bernardi et al.[25] compared different techniques to solve the EM field outside the plasma discharge. Three different techniques were compared namely: the standard vector potential formulation (ST); magnetic dipole boundary conditions, and the EF boundary conditions. The authors found that, out of the three methods investigated, the EF model reduces the computational time by 60% than the other two methods. The authors have compared the radial distribution of the electric field using all the three models. They found that, though in the plasma region the distributions of electric field were nearly the same, closer agreement was observed

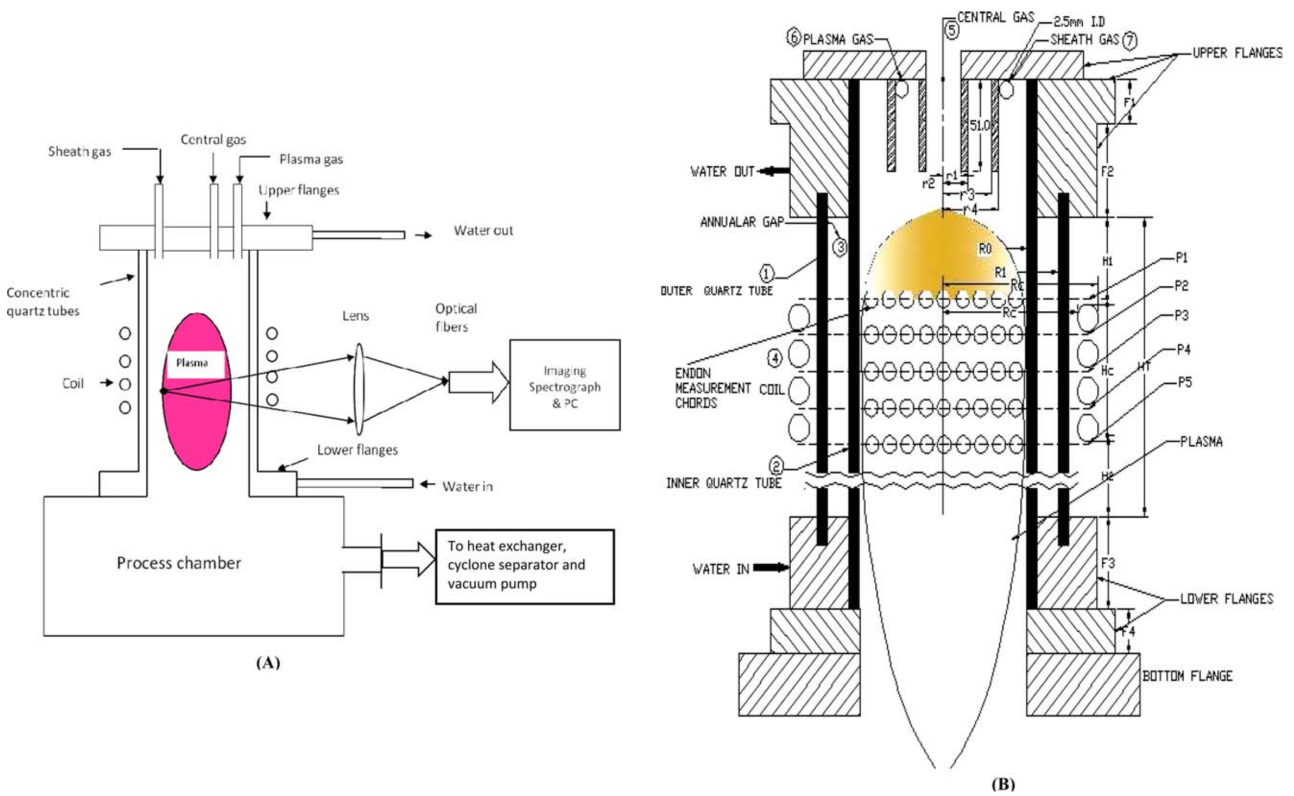

Figure 1. A schematic representation of experimental setup.

(A) Experimental assembly, (B) schematic of plasma torch, (1) outer quartz tube, (2) inner quartz tube, (3) annular gap, (4) coil turns, (5) central gas inlet, (6) plasma gas inlet, and (7) sheath gas inlet. [Color figure can be viewed in the online issue, which is available at wileyonlinelibrary.com.]

with the prediction of the ST model. The method was later extended for 3-D cases and improved agreement was obtained. The focus of the work of Bernardi et al.[25] was on comparison of numerical methods with the ST method as the exact method of formulation. However, the authors did not compare the predictions of different mathematical techniques with the experimental data published in the literature. Further, a laminar model was considered for the study.

Motivation

From the foregoing discussion, it can be seen that, in the published literature, the researchers have mainly focused on temperature measurements mostly above and below the coil region in an ICP system and not in the coil region. Also, except Boulos[21] and Nishiyama et al.[23] experimental data has not been compared with model predictions. Further, Boulos[21] compared velocity distribution in radial direction and Nishiyama et al.[23] measured axial temperature distribution. Although complexity can be reduced by implementation of simpler boundary conditions for the vector potential equations as shown by various researchers,[22,23] good results are provided by the ST approach as well. Investigations have been made by varying the central gas flow rate and the total gas flow rate. However, no attempt has been made to vary the sheath gas flow rate and observe temperature and velocity distributions. The motivation for the present investigation is as follows: (1) to undertake systematic measurements of temperature profiles in the coil region at various axial locations (Table 4); (2) to carry out experimental measurements for different sheath gas flow rates and over a wide range of power; (3) present a 2-D axisymmetric CFD simulation for the real turbulent case with the ST approach; and (4) to compare the model predictions with experimental measurements reported in the published literature as well as with those performed in the present model.

Experimental Setup and Measurements

Experimental setup

The ICP torch used in the present work was powered by a 50 kW RF oscillator working at 3 MHz. It was operated at near atmospheric pressure. Figure 1A shows the schematic of the ICP torch. Position of the coil and gas introduction points are also shown in Figure 1A. The corresponding dimensions have been given in Table 3. The ICP torch consists of two concentric quartz tubes (1,2) with inner diameter (ID) and outer diameter (OD) of the inner tube are 60 and 65 mm and the ID and OD of the outer tube are 74 and 80 mm, respectively. Cooling water is flown through the annular gap of 4.5 mm (3) shown in Figure 1A. Outer tube is surrounded by a water-cooled induction coil, having four turns (4). The gases are introduced in the quartz tube from the top. The central gas (5) is introduced in axial direction along the center line of the torch. The plasma gas (6) and sheath gas (7) are introduced through two holes of 2.5-mm diameter located at distances r_2 and r_3, respectively. The gases are introduced almost tangentially (at an angle of 20° downward) to get a helical flow. Plasma gas and sheath gas enter in the opposite directions. A metallic cylinder (8) of 51-mm length, 44-mm ID, and 50-mm OD separates the sheath and plasma gases. The sheath gas creates a cold buffer zone between the plasma (9) and quartz tube and protects it from melting. We have

Table 3. Dimensions of Experimental Setup

Parameters	Values
r_1	1.00 mm
r_2	6.45 mm
r_3	22.3 mm
r_4	25 mm
R_0	30.0 mm
R_1	40.0 mm
R_C	55.0 mm
R_{C1}	60 mm
f	3.0 MHz
H_1	166.0 mm
H_2	114.0 mm
H_C	70.0 mm
H_T	350. 00 mm
F1	12 mm
F2	55 mm
F3	55 mm
F4	12 mm

Table 4. Axial Positions of ICP Torch for Spectroscopic Measurements

Symbol	Distance from upper flange, *z* (mm)
P_1	220
P_2	248
P_3	268
P_4	288.4
P_5	308

used Argon as plasma gas and sheath gas, and we have not used any central gas. The torch is vertically mounted on a process chamber, which is evacuated by a rotary vacuum pump through a heat exchanger, a cyclone particle separator, and a filter, as shown in Figure 1B. The pressure in the chamber can be maintained at any desired value from about 100 to 1000 mB by means of a pressure sensor and a feedback control valve. We have maintained the pressure in the chamber very near to 1000 mB. To measure plasma temperature by optical emission spectroscopy, optical data was collected at five planes viz. P1–P5 as shown in Figure 1A. Location of these planes is given in Table 4.

1. The quartz tube that contains plasma was highly transparent. Therefore, the intensity of the direct light from plasma is orders of magnitude higher than the reflected light from surfaces of the quartz tubes. The copper coil was coated with Teflon having a rough surface finish. As a result, the scattered light from the edges of the coil is of much lower intensity as compared to the emissions from the plasma reaching directly to the lens.
2. Temperature measurement using Boltzmann plot method
3. The Boltzmann plot method[26] was used for the determination of plasma temperature. A typical Boltzmann plot is shown in Figure 2A. Slope of the straight line shown in the graph gives the plasma temperature. This technique requires relative measurement of emission lines intensities. There are about 17 strong Ar–I emission lines with well-separated energy levels in wavelength range of 680–890 nm. A 1200 lines/mm reflection grating blazed at 500 nm was used as dispersive element in the spectrograph. Grating response and the quantum efficiency of charge coupled device (CCD) put together give almost a flat instrument response in this wavelength range. Therefore, this wavelength range was chosen to determine the plasma temperature. ICP was imaged by a lens and a linear array of nine fibers placed in the image plane. The fibers were positioned in a horizontal plane so that the nine chordal intensities (line integrated intensities along nine chords) at one horizontal cross-section of the plasma can be recorded. This is known as end-on measurement of intensity along a chord. These nine chords of the circular cross-section of the plasma at one of the planes P1–P5 are shown in Figure 2B. The lens and the nine optical fibers are adjusted in such a way that the image of the plasma falls on the fibers symmetrically. Care was taken that the center of the image fell on the 5th fiber. An imaging spectrograph (Shamraock-SR-303 I, with ANDOR CCD) was used to measure the intensity of Ar–I lines.
4. Using Abel inversion technique,[27,28] the chordal intensities were inverted to radial intensity profiles at that axial location. The intensity data were fitted in the Boltzmann plot and the radial temperature profiles were obtained. This procedure was repeated for five axial positions. These data were used to get axial temperature profiles. The power fed to the torch and gas flow rates were varied and their effect on the temperature profiles was investigated. A short theory of this technique follows: assuming that the plasma is in local thermodynamic equilibrium (LTE) and is optically thin, the intensity of an atomic emission line (I_{ul}) is related to excitation energy, population density of upper state (n_u), and the transition probability (A_{ul}) by the following equation[27]

$$I_{ul} = \left(\frac{1}{4\pi}\right) A_{ul} n_u h \nu_{ul} L \tag{1}$$

Here, I_{ul} denotes intensity of the atomic emission line, A_{ul} denotes transition probability between the upper level u and

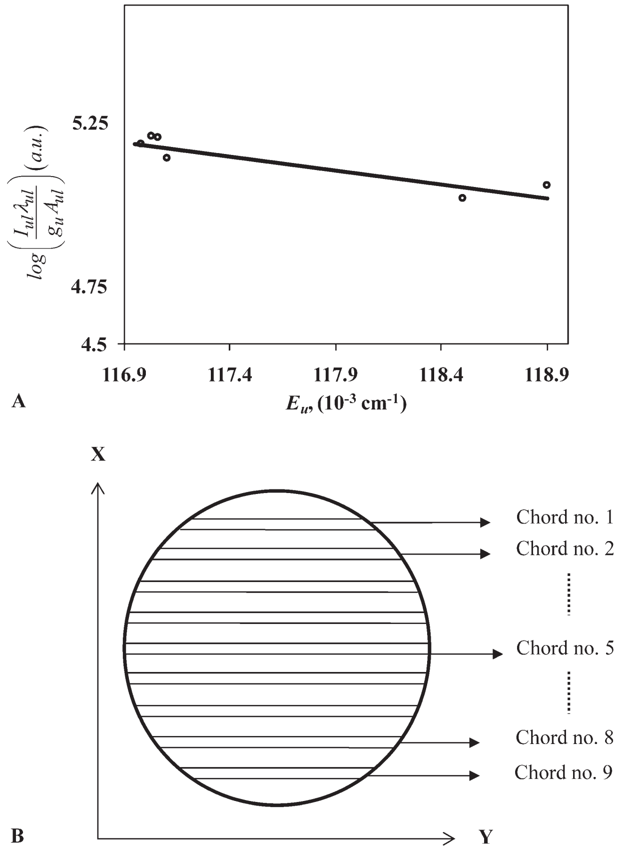

Figure 2. (A) A typical Boltzman plot and (B) cross section of plasma reactor and location of chords.

Fibers collect integrated light along the chords.

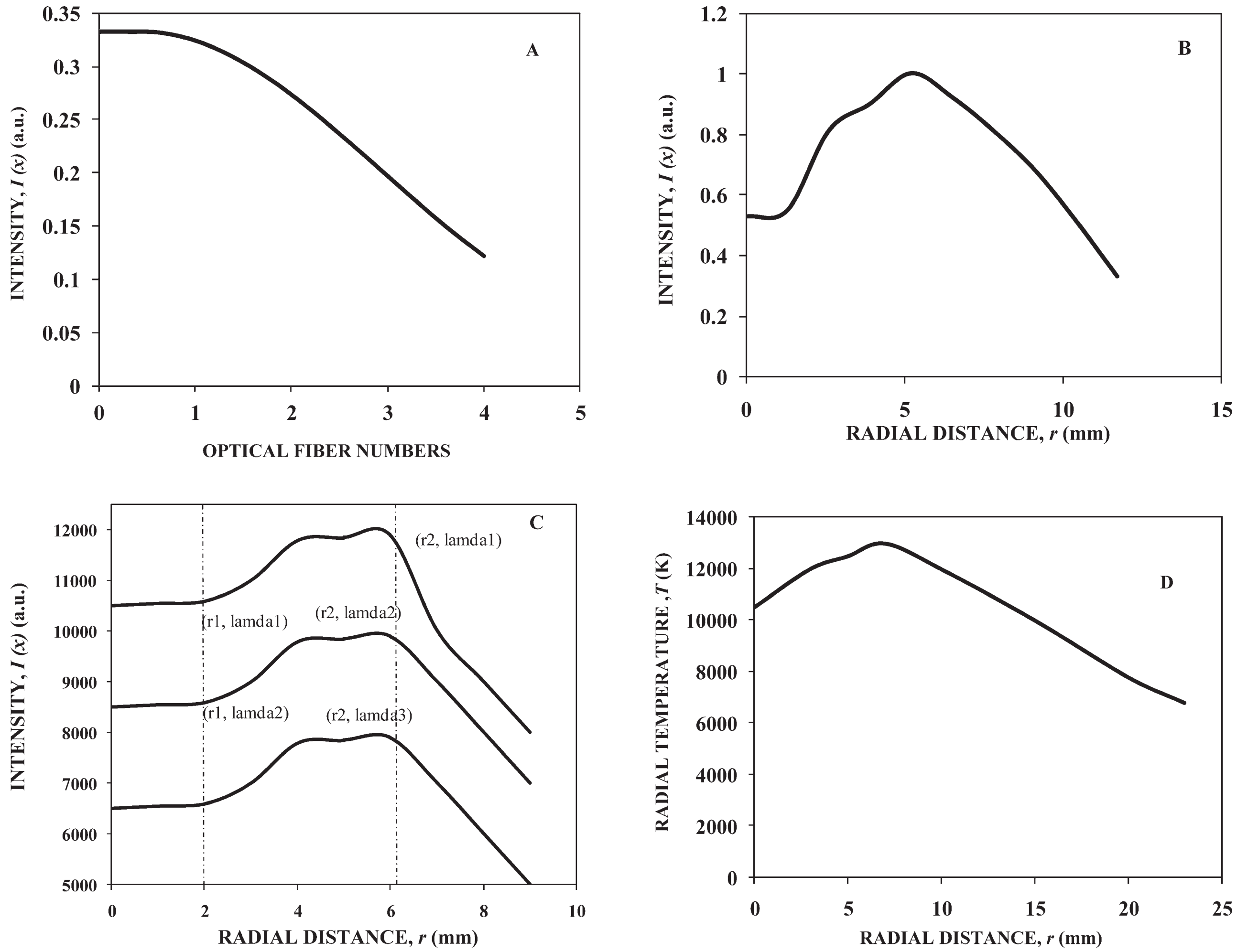

Figure 3. (A) Typical chordal intensity *I* (*x*) for a spectral line, (B) typical radial intensity profile of a spectral line after Abel inversion, (C) typical radial intensity profiles for a number of spectral lines, and (D) typical radial temperature profile at a cross section of the ICP torch.

the lower level l, n_u denotes population density of atoms excited to the upper energy level, h denotes Planck constant, v_{ul} denotes frequency of radiation, and L denotes optical path length.

Ratio of density of atoms excited to upper level to that of the lower level is given by the following Maxwell–Boltzmann formula[29]

$$\frac{n_u}{n_l} = \frac{g_u}{g_l} e^{\left(-\frac{E_u}{kT}\right)} \tag{2}$$

Substitution of n_u from Eq. 2 in Eq. 1 and subsequent rearrangement gives

$$\ln\left(\frac{I_{ul}\lambda_{ul}}{g_u A_{ul}}\right) = B - \frac{E_u}{kT} \quad \text{where } B = \ln\left(\frac{hcn_l L}{4\pi g_l}\right) \text{is a constant} \tag{3}$$

The values of I_{ul} were measured using the spectrograph and the values of λ_{ul}, g_u, A_{ul}, and E_u were taken from the literature.[16] If $\ln(I_{ul}\lambda_{ul}/g_u A_{ul})$ is plotted against E_u for several spectral lines (all must be Ar–I lines) reciprocal of the slope of the straight line plot gives the temperature as in Eq. 3.

Measurement procedure

A typical chordal intensity profile (obtained for one spectral line) is shown in Figure 3A. Assuming plasma to be cylindrically symmetric, chordal intensity data were converted into a radial intensity profile for each line by Abel inversion technique[27,28] (Figure 3B). At $r = 0$, Abel Inversion leads to singularity. Value of intensity $I(r, \lambda)$ at $r = 0$ was extrapolated from the graph of $I(r, \lambda)$ with $r \neq 0$. After determining radial intensity profiles for more than 10 spectral lines, the relative intensity data at one radial distance was used as an input (as shown in Figure 3C) to Boltzmann plot and the value of temperature at that location was determined. The procedure was repeated, at a number of radial locations to obtain the radial temperature profiles, and these are shown in Figure 3D. Figure 3D is a typical radial temperature profile. At low power, we observed temperature peaks near the axis and as the power increases the peak shifted to the wall depending on the skin depth. This procedure was repeated for five axial positions as mentioned in Table 4.

Mathematical modeling

During the past 25 years, CFD is being increasingly used because of the developments in the computational power as well as numerical techniques (Joshi and Ranade[30]; Ekambara et al.[31]). Further, the CFD predictions are being validated by experiments (for instance, Murthy and Joshi[32]). In the published literature, the knowledge of flow patterns has been successfully used for the estimation equipment performance

Table 5. Governing Equations in Cylindrical Coordinates for Axisymmetric Flow

Property	Equations
Continuity	$\frac{1}{r}\frac{\partial}{\partial r}\langle ru_r\rangle+\frac{\partial}{\partial z}\langle u_z\rangle=0$
Axial velocity momentum	$\langle u_z\rangle\frac{\partial\langle u_z\rangle}{\partial z}+\frac{1}{r}\langle u_r\rangle\frac{\partial\langle ru_z\rangle}{\partial r}=-\frac{1}{\rho}\frac{\partial\langle p\rangle}{\partial z}+(v+v_t)\left[\frac{1}{r}\frac{\partial}{\partial r}\left(\frac{\partial\langle ru_r\rangle}{\partial r}\right)+\frac{\partial}{\partial z}\left(\frac{\partial\langle u_z\rangle}{\partial z}\right)\right]+F_z$
Radial velocity momentum	$\frac{1}{r}\langle u_r\rangle\frac{\partial\langle ru_r\rangle}{\partial r}+\langle u_z\rangle\frac{\partial\langle u_r\rangle}{\partial z}=-\frac{1}{\rho}\frac{\partial\langle p\rangle}{\partial z}+(v+v_t)\left[\frac{1}{r}\frac{\partial}{\partial r}\left(\frac{\partial\langle ru_r\rangle}{\partial r}\right)+\frac{\partial}{\partial z}\left(\frac{\partial\langle u_z\rangle}{\partial z}\right)-\frac{u_r}{r^2}\right]+F_r$
	where, $F_r=\frac{1}{2}\mu_0\sigma\,\mathrm{Real}\left[E_\theta H_z^*\right]$; $E_\theta=-\mathrm{i}\omega A_\theta$; s and $\mu_0H_r=-\frac{\partial}{\partial z}(A_\theta)$
Energy	$\frac{1}{r}\frac{\partial\langle u_rH\rangle}{\partial r}+\frac{\partial\langle u_zH\rangle}{\partial z}=\frac{1}{r}\frac{\partial}{\partial r}\left[r\alpha_{\mathrm{eff}}\frac{\partial\langle H\rangle}{\partial r}\right]+\frac{\partial}{\partial z}\left[\alpha_{\mathrm{eff}}\frac{\partial\langle H\rangle}{\partial z}\right]+U_{\mathrm{P}}+U_{\mathrm{R}}\ U_{\mathrm{P}}=\frac{1}{2}\sigma\left[E_\theta E_\theta^*\right];\ U_{\mathrm{R}}=5600(T-9500)+181(T-9500)^2$
Turbulent kinetic energy	$\frac{1}{r}\langle u_r\rangle\frac{\partial(r\kappa)}{\partial r}+\langle u_z\rangle\frac{\partial\kappa}{\partial z}=\left(v+\frac{v_t}{\sigma_\kappa}\right)\left[\frac{1}{r}\frac{\partial}{\partial r}\left(\frac{\partial(r\kappa)}{\partial r}\right)+\frac{\partial}{\partial z}\left(\frac{\partial\kappa}{\partial z}\right)\right]+G_\kappa-\rho\varepsilon$
	Turbulent kinetic energy $G_\kappa=v_t\lvert\overline{S}\rvert^2$where $\lvert\overline{S}\rvert=\sqrt{2\overline{S_{ij}S_{ij}}}$ and $\lvert\overline{S_{ij}}\rvert=\frac{1}{2}\left(\frac{\partial\langle u_z\rangle}{\partial r}+\frac{\partial\langle u_r\rangle}{\partial z}\right)$
Energy dissipation rate equation	$\frac{1}{r}\langle u_r\rangle\frac{\partial(r\varepsilon)}{\partial r}+\langle u_r\rangle\frac{\partial\varepsilon}{\partial r}=\left(v+\frac{v_t}{\sigma_k}\right)\left[\frac{1}{r}\frac{\partial}{\partial r}\left(\frac{\partial(r\varepsilon)}{\partial r}\right)+\frac{\partial}{\partial z}\left(\frac{\partial\varepsilon}{\partial z}\right)\right]+C_1\frac{\varepsilon G_k}{k}-C_2\frac{\rho\varepsilon^2}{k}\ C_1=1.44,\ C_2=1.92$
Vector potential equation	$\frac{\partial^2A_{\mathrm{R}}}{\partial z^2}+\frac{1}{r}\frac{\partial}{\partial r}\left(r\frac{\partial A_{\mathrm{R}}}{\partial r}\right)-\frac{A_{\mathrm{R}}}{r^2}+\mu_0\omega\sigma A_{\mathrm{I}}=0\ \frac{\partial^2A_{\mathrm{I}}}{\partial z^2}+\frac{1}{r}\frac{\partial}{\partial r}\left(r\frac{\partial A_{\mathrm{I}}}{\partial r}\right)-\frac{A_{\mathrm{I}}}{r^2}-\mu_0\omega\sigma A_{\mathrm{R}}=0\ A_\theta=A_{\mathrm{R}}+iA_{\mathrm{I}}$

(For instance, for solid suspension by Murthy et al.[32]). Therefore, it was thought desirable to use the CFD tool for understanding the performance of plasma reactors. The following assumptions have been made:

Assumptions

1. Flow field is affected by the local plasma temperature changes
2. System is axially symmetric (Figure 1B)
3. Steady state, incompressible, turbulent flow
4. Negligible viscous dissipation
5. Local thermodynamic equilibrium
6. Volumetric power input due to ohmic heating
7. Radiation heat losses can be treated as a volumetric heat sink
8. The plasma is optically thin
9. Negligible displacement currents

A special mention needs to be emphasized on the assumption of LTE. Since the plasma is at near atmospheric pressure, it is collision dominated and LTE is assumed to be valid.[34] One of the most important physical parameters defining the state of plasma is its temperature, which represents distribution of kinetic energy of the species (electrons, ions, neutral atoms, molecules, and photons) constituting the plasma. Thus, there are several species in the plasma together with several degrees of freedom. Temperature specific to one species and for a particular degree of freedom may be stated as follows:

T_{kin}—(kinetic temperature) corresponds to translational motion of particles.

T_{exe}—(excitation temperature) that shows how the electronic excited states are distributed.

T_{ion}—(ion temperature) that shows translational temperature of ions.

T_{e}—(electron temperature) is translational temperature of electrons.

T_{nu}—(neutral atom temperature) is translational temperature of neutral atoms

T_{rot}—(rotational temperature) that is a measure of how rotational levels of molecules or radicals are distributed.

Plasmas are composed of species with very large mass differences viz. electrons and heavy particles like ions, neutral atoms, and molecules. Due to high mobility of electrons, they extract energy from EM field very quickly. Heavy ions get a small fraction of energy as compared to electrons due to their low mobility. Therefore, T_{e} and T_{ion} can be different in plasma. In LTE, all temperatures described earlier (except radiation temperature) are equal, and thus, only one temperature is required to characterize the plasma. Thermal plasmas have high-specific enthalpies, high-particle densities (typically above $10^{16}/\mathrm{m}^3$) and can have high flow velocities (~few hundred m/s). The ICP belongs to the category of thermal plasmas with low velocities (~few m/s).

It may be noted that the thermal nonequilibrium is relatively more significant in low pressure plasmas upto 300 mbars and not for atmospheric pressures (Mostaghimi et al.[35]). Mostaghimi et al.[35] have considered two cases (1) An ICP torch operating at 1000 mbar and (2) An ICP torch operating at 300 mbar conditions. For each case, the authors used two models (a) without the governing equations for continuity and energy equations for electrons and heavy particles (LTE model) and (b) with the above equations in addition to the governing equations for fluid flow (non-LTE model). The plasma gas flow rates and sheath gas flow rates were 3 and 34 lpm, respectively. The radial temperature distribution for various axial positions showed that at 1000 mbar conditions the LTE model and non-LTE model showed good agreement (within 1%) in the bulk region, while near the wall and entrance region of the torch the deviations were around 10%. However, for the second case for a pressure 300 mbar, the deviations between the two models were 20% in the bulk region, while they were around 30% in the wall region. Several works on low pressure plasmas (less than 100 mbar) use the thermal nonequilibrium models (Ye et al.,[9] Johannes et al.,[36] Panagopoulos et al.,[37] and Economou[38]). In the present work, the gas pressure is 1000 mbar. Further, it may be emphasized that the investigations have been performed, mostly in the bulk region and the coil region where, thermal equilibrium prevails and the deviations between the LTE and the non-LTE models have been found to be less than 1%. The case considered here does not consider the regions in the entrance or wall regions.

In addition to this, temperature is ~10,000 K. If one applies Saha equation[39] at this temperature, less than about 0.1% gas is ionized. This means, in the present case, plasma can be treated very near to a hot gas. Hence, the continuity, momentum,and energy conservation equation for electron and ions is not applicable and hence not included in the analysis. The governing equations have been listed in Table 5.

Governing equations and boundary conditions

The continuity, momentum, energy, and vector potential equations are solved for optically thin plasma using 2-D model. The set of governing equations of RF-ICP is simulated within FLUENT environment. The vector potential equations are solved using user defined scalar.

The boundary conditions are as follows:

- Inlet conditions ($z=0$)

$$u_z=\begin{cases} Q_1/\pi r_1^2 & r<r_1 \\ 0 & r_1\le r\le r_2 \\ Q_2/\pi\left(r_3^2-r_2^2\right) & r_2\le r\le r_3 \\ 0 & r_3\le r\le r_4 \\ Q_3/\pi\left(R_0^2-r_4^2\right) & r_4\le r\le R_0 \end{cases} \tag{4}$$

$$u_r=0 \tag{5}$$

$$T=300\,\mathrm{K} \tag{6}$$

$$\frac{\partial A_\mathrm{R}}{\partial z}=\frac{\partial A_\mathrm{I}}{\partial z}=0 \tag{7}$$

$$\kappa=0.005(u_z^2+u_0^2) \tag{8}$$

$$\varepsilon=0.1\kappa^2 \tag{9}$$

- Centerline ($r=0$)

$$\frac{\partial u_z}{\partial r}=u_r=\frac{\partial H}{\partial r}=\frac{\partial \kappa}{\partial r}=\frac{\partial \varepsilon}{\partial r}=A_\mathrm{R}=A_\mathrm{I}=0 \tag{10}$$

- Wall ($r=\mathrm{R0}$)

$$u_z=u_r=k=\varepsilon=0 \tag{11}$$

$$\lambda\frac{\partial T}{\partial r}=\frac{\lambda_\mathrm{w}}{\delta_\mathrm{w}}(T_\mathrm{s}-T_\mathrm{w}) \tag{12}$$

$$A_\mathrm{R}=\frac{\mu_0 I}{2\pi}\sqrt{\frac{R_\mathrm{c}}{R_0}}\sum_{i=1}^{\mathrm{coil}}G(k_i^{'})+\frac{\mu_0\omega}{2\pi}\sum_{p=1}^{\mathrm{C.V.}}\sqrt{\frac{r_p}{R_0}}\sigma_p A_{I,p}S_p G\left(k_p^{'}\right) \tag{13}$$

$$A_\mathrm{I}=-\frac{\mu_0\omega}{2\pi}\sum_{p=1}^{\mathrm{C.V.}}\sqrt{\frac{r_p}{R_0}}\sigma_p A_{\mathrm{R},p}S_p G\left(k_p^{'}\right) \tag{14}$$

where

$$G\left(k^{'}\right)=\frac{(2-k^{'2})K(k^{'})-2E(k^{'})}{k^{'}} \tag{15}$$

$$k_p^{'2}=\frac{4R_0 r_p}{(r_p+R_0)^2+(z_b-z_p)^2},\quad k_i^{'2}=\frac{4R_i R_0}{(R_i+R_0)^2+(z_i-z_b)^2} \tag{16}$$

- Exit

$$\frac{\partial u_z}{\partial z}=\frac{\partial u_r}{\partial z}=\frac{\partial H}{\partial z}=\frac{\partial A_\mathrm{R}}{\partial z}=\frac{\partial A_\mathrm{I}}{\partial z}=\frac{\partial \kappa}{\partial z}=\frac{\partial \varepsilon}{\partial z}=0 \tag{17}$$

Numerical procedure

The schematic of the experimental geometry is shown in Figure 1. A nonuniform grid (as shown in Figure 5) was generated using GAMBIT. A 2-D nonuniform colocated grid was used to solve the governing equations using control volume technique. The semiimplicit method for pressure linked equations algorithm developed by Patankar[40] was used to solve the pressure velocity coupling. Continuity, momentum, energy, and vector potential equations were discretized using upwind scheme. The under-relaxation scheme is used for dependent variables. The user defined function code was developed for the experimental geometry. The code was simulated using turbulent flow model for experimental geometry. For turbulent flow, standard $\kappa-\varepsilon$ model was used to solve the turbulent kinetic energy and the turbulent dissipation energy. The standard k–ε model parameters (Launder and Spalding[41]) are $C_\mu=0.09$, $C_1=1.44$, $C_2=1.92$, $\sigma_\kappa=1.0$, $\sigma_\varepsilon=1.30$, and $\sigma_t=0.85$. The convergence criterion used was that the residual should be less than 1×10^{-5}.

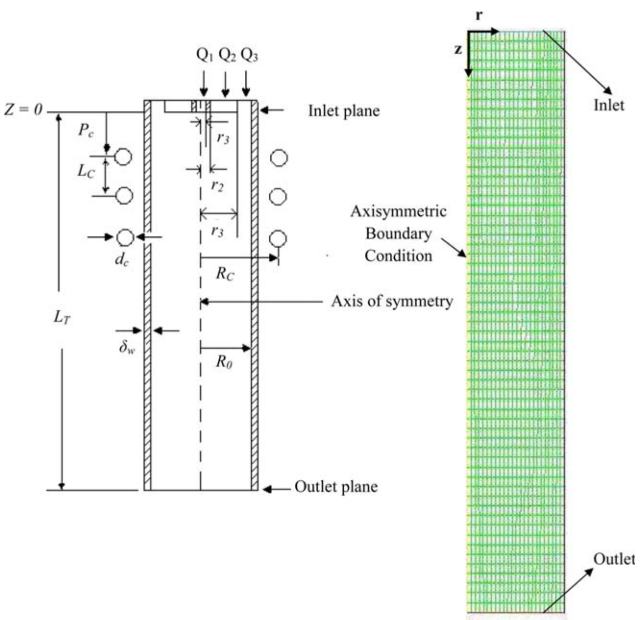

Figure 4. Details of the geometry of Mostaghimi et al.

(A) Schematic of the geometry and (B) Sample grid. [Color figure can be viewed in the online issue, which is available at wileyonlinelibrary.com.]

Grid sensitivity

The details of the geometry used by Mostaghimi and Boulos[22] and the grids have been shown in Figures 4A, B, respectively. The grid sensitivity was tested for the geometry and conditions considered by Mostaghimi and Boulos.[22] In 2-D simulations, three grid sizes have been considered (6000, 12,000, and 24,000). Grid independence was tested by monitoring the variables and residuals during the iteration process. The axial velocities at centerline axial direction have been compared for the three grids. Figure 6A shows only 2% deviation for the three grids and hence the lowest grid (with number of mesh cells 6000) has been selected for all the simulations. The details of the grid of the present experimental geometry have been shown in Figure 5. For the grid sensitivity of the present experimental setup, three grid sizes were chosen (63,000, 126,000, and 189,000). Since the deviations were found to be around 2%–3% (Figure 6B), the lowest grid size of 63,000 was used for all the simulations of geometry covered in this work.

Results and Discussion

Comparison of the present CFD simulations with those published in the literature

We first validate the present CFD simulation with the geometries and the parameters covered in the most prominent works available in the published literature. We first present a comprehensive comparison of laminar models with Boulos[21] and Mostaghimi and Boulos.[22] Then the simulations will be compared with the experimental results of Lesinski et al.[41]

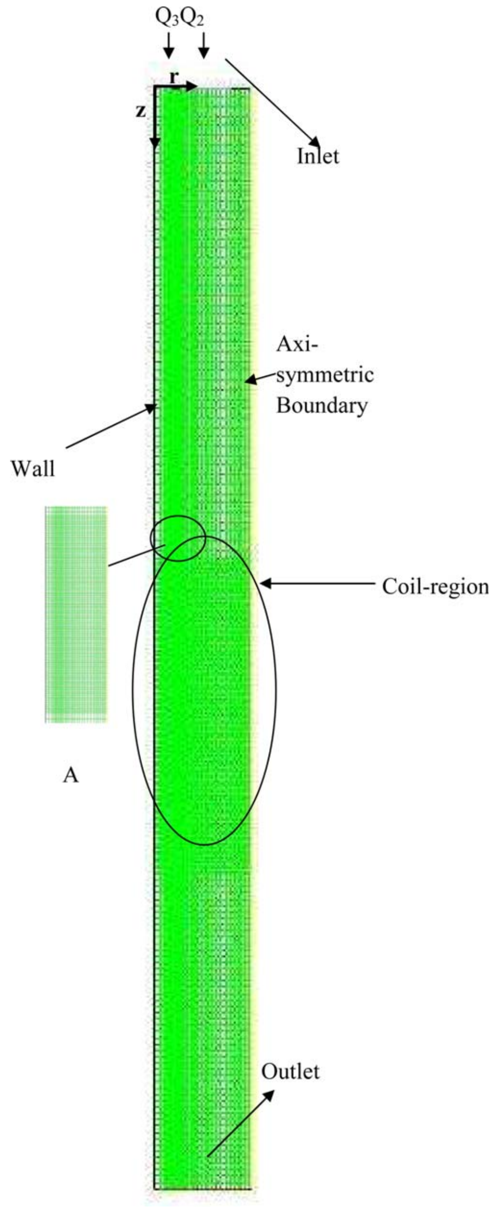

Figure 5. Sample grid considered for simulations.

(A) Zoomed portion of the fine mesh in the coil region. [Color figure can be viewed in the online issue, which is available at wileyonlinelibrary.com.]

and Watanabe et al.[43] In the next subsection, we present the simulations for the turbulent flow and compare the model predictions with all the experimental results from the present work as well as all the results from the published literature.

Temperature profiles

Figure 7A shows the temperature profiles for three different cases.[20,22,24] Excellent agreement (within 3%) can be seen with the geometry of Mostaghimi and Boulos[22] (2-D model for momentum and also the EM equations are solved in both *r* and *z* directions). The simulations were compared with the predictions of Mostaghimi et al.[20] where 1-D model was used for EM equations, while 2-D model was used for the continuity momentum and energy equations. In this case, the agreement can be seen to be within 10%–15%, and with some systematic deviation (Figure 7A). This is because of the EM equations are solved only in single dimension. The model predictions have then been compared with the predictions reported by Xue et al.[24] and Mostaghimi and Boulous[22] (where the EM equations, continuity, momentum, and energy were solved in both *r* and *z* directions as in the present case) and good agreement can be seen with deviations within 4% (Figure 7A).

The axial temperature profiles of Watanabe et al.[43] and model predictions of Nishiyama et al.[23] have been compared with the present model and shown in Figure 7B. Nishiyama et al.[23] underpredict the experimental measurements by 10%–12%, whereas the present model agrees within 6% deviation. The under predictions of Nishiyama et al.[23] can be attributed to the coarse grid sizes and the Runge–Kutta method used for the CFD simulations.

Velocity profiles

Researchers have observed that, near the coil region, the plasma velocity profiles are similar to those observed in the case of a free jet with a peak velocity magnitude at the center. Further downstream, the profiles become increasingly

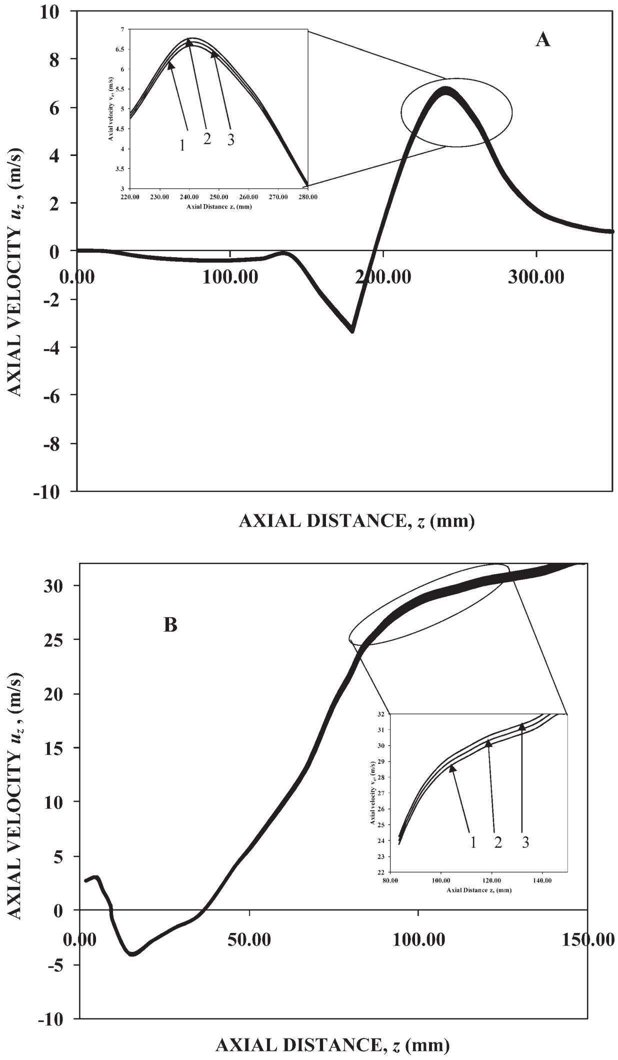

Figure 6. Variation of axial velocity with axial distance for three different grid sizes.

(A) Geometry of Mostaghimi et al.[20] (1) 6000 cells (2) 12,000 cells (3) 24,000 cells (B) Geometry for the present experimental setup (1) 63,000 cells (2) 126,000 cells (3) 189,000 cells.

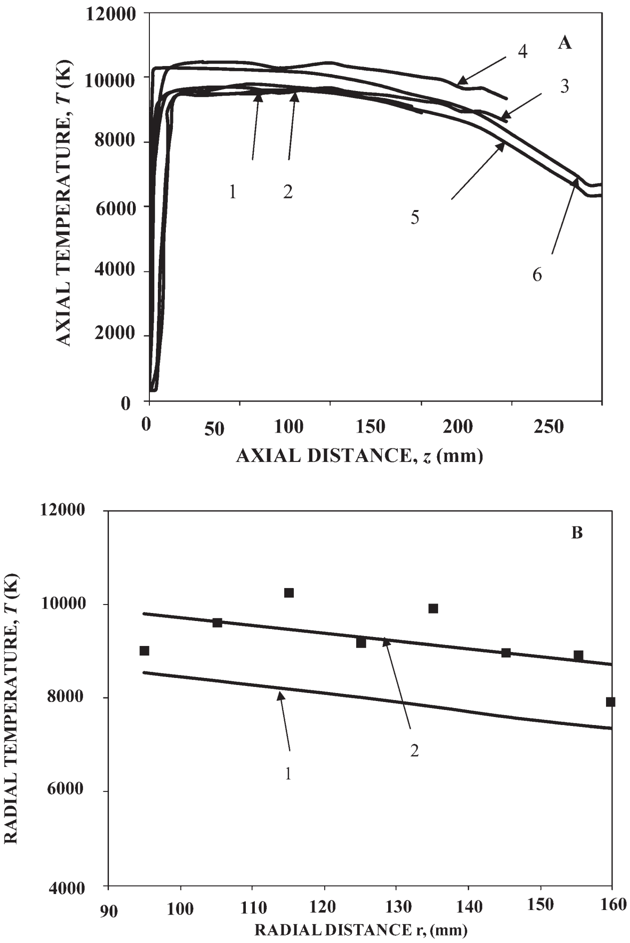

Figure 7. Comparison of axial temperature profiles for various literature cases with the present CFD predictions.

(A) Model predictions of literature (1) Mostaghimi and Boulos[22] (2) Present model (3) Mostaghimi et al.[20] (4) Present model (5) Xue et al.[24] (6) Present model and (B) Comparison with experimental data of literature (1) Nishiyama et al.[23] model (2) Present model ■ Experimental data of Watanabe et al.[43]

flat with mean velocity dropping rather slowly. Figure 8A shows the axial profiles of the axial velocity predicted by the present model and those of Mostaghimi and Boulos[22] and Xue et al.[24] Excellent agreement can be seen with minor over-predictions of around 6%. Figure 8B shows the axial velocity profiles of Nishiyama et al.[23] for various power inputs ($P = 5$, 7, and 8 kW) together with the predictions of the present model. The geometry and conditions have been kept the same as that of Nishiyama et al.[23] and again excellent agreement (within 8%) can be seen in Figure 8B. The present model has also been compared with the experimental data of Lesinski et al.[42] and Figure 9 shows excellent agreement at all the axial locations.

Experimental results of the present work and comparison with CFD predictions

Radial Temperature Profiles. In the present work, five different RF powers in the range of 3–14 kW were used. Further, for each RF power, the effect of sheath gas flow was investigated at two levels: 10 and 25 lpm. A typical spectrum of Ar–I is shown in Figure 10A. Figure 10B shows a typical spectrum collected by nine optical fibers at one axial location.

Effect of Power Input and Sheath Gas Flow Rate. Three sets of powers (4.73, 8.84, and 13.35 kW) have been investigated for the sheath gas flow rate (Q_3) of 10 lpm and plasma gas flow rate (Q_2) of 3 lpm. The measurements have been performed at five axial locations in the coil region as given in Table 4. The plasma gas and sheath gas were found to be in a well-mixed state, when it reaches the coil region (in the axial direction). The ionization of the plasma gas in the coil region is maximum at a certain distance from the plasma boundary. This distance is called the skin depth (δ). The skin depth depends on the magnetic permeability, electrical conductivity, and the oscillator frequency (Boulos,[21] and Mostaghimi and Boulos[22]). The electrical conductivity depends on the electron density and the excitation temperature (Joshi et al.[18]) of the plasma. Thus, a maximum temperature is observed where maximum electron deposition takes place and the excitation temperature is the highest. The skin depth is also a strong function of sheath gas flow rate and

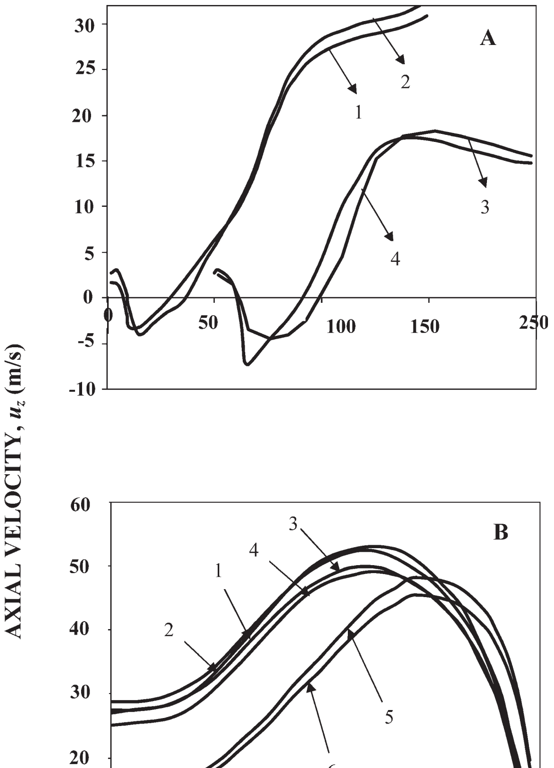

Figure 8. Comparison of axial velocities for various literature cases with the present CFD predictions.

(A) Axial velocity profiles(1) Mostaghimi and Boulos[22]; (2) Present model; (3) Xue et al.[24]; (4) Present model. (B) Axial velocity profiles for different powers considered by Nishiyama et al.[23] (1) Nishiyama et al.,[23] $P = 5$ kW; (2) Present model; (3) Nishiyama et al.,[23] $P = 7$ kW; (4) Present model; (5) Nishiyama et al.,[23] $P = 8$ kW; (6) Present model.

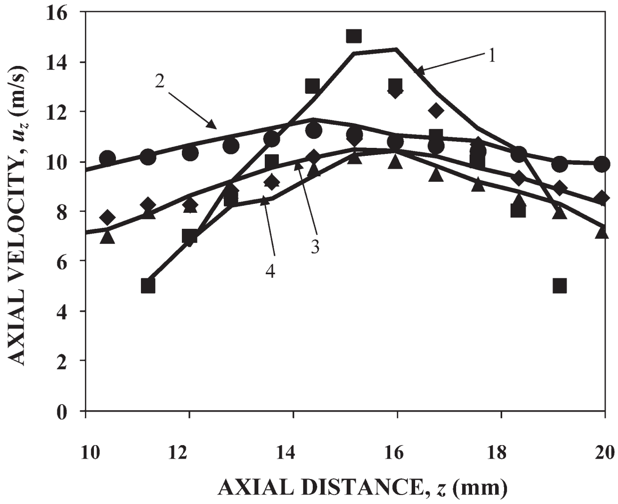

Figure 9. Comparison of experimental data of Lesinski et al.[40] with present model predictions for various axial locations.

Present CFD predictions: (1) $z = 10$ mm; (2) $z = 33$ mm; (3) $z = 58$ mm; (4) $z = 82$ mm; Experimental points of Lesinski et al.[40]: ■ $z = 10$ mm; ▲ $z = 33$ mm; ◆ $z = 58$ mm; • $z = 82$ mm

the power input. Here, for the conditions chosen in the present work, we have made an attempt to measure the radial temperature profiles at different axial locations in the coil region. Figure 11A shows the profile at $z = 153.1$ mm, the temperature peak was found to be away from the central line. The gas temperature can be seen to increase gradually toward the wall and attains a maximum at a distance $\delta_1 = 5.17$ mm from the plasma boundary and then decreases. For the same axial position, with an increase in the power input, the maximum temperature peak was found to move away from the center. For example, for a power input of 8.84 and 13.35 kW, the peaks are at distances of $\delta_2 = 4.0$ mm and $\delta_3 = 3.5$ mm, respectively, from the plasma boundary. Obviously, the temperature levels were found to increase with an increase in the power input. As the power level increases, the electrical conductivity of the plasma increases with a corresponding increase in the skin depth resulting in the movement of the peak away from the centerline toward the wall. Beyond the peak value, the temperature steadily decreases. This is due to the decrease in both convective heat transfer and electrical conductivity. The reason for decrease in electrical conductivity is due to the decrease in the power coupled to plasma beyond maximum power deposition region. Therefore, electrical conductivity also decreases slowly toward the wall. The observation of this particular behavior of radial temperature with power input for a constant value of Q_3 is one of the important results of the present work.

The exercise described in the above paragraph was repeated for different axial positions in the coil region. Table 6 shows the various values of skin depths for different power inputs and the sheath gas flow rates. It can be seen that the skin depth decreases with an increase in the power. Radial temperature profile for axial position P1 is shown in Figure 11B. For the lowest power, the skin depth value for position P2 ($z = 170.2$ mm) is higher than for axial position P1 ($z = 153.1$ mm). This shows that the region of highest power deposition varies axially for a particular power input. From Table 6, it is evident that the skin depth increases with respect to the axial position for all power inputs till position P3 and then it decreases. Further, Figures 11A–E also show the comparison of the CFD predictions with the experimental measurements. The CFD predictions can be seen to agree very well with the experimental data. As seen in Figure 11A, for axial position P1 and for the case of low power input (4.73 kW), the agreement is within 5% while for slightly higher power input the agreement is within 8%. As we move axially downward (axial locations P2 and P3), the agreement is within 7%–8%, especially, at regions where the temperature gradients are high. This feature was found to be true for all the power inputs under consideration. For axial position P3, the agreement upto 8% can be observed in the region of skin depth. For axial locations P4 and P5, the predictions are better (3%–5% of the experimental values).

The sheath gas flow rate was further increased to 25 lpm and a new set of power inputs were selected namely 5.24, 9.26, and 13.74 kW. Figures 12A–E show the radial temperature profiles for ICP with 3 lpm plasma gas flow rate and 25 lpm sheath gas flow rate. In this case too, as the power increases, the peak temperature also increases and the temperature decreases as we move toward the wall. At axial locations P3 and P4, we observe that the temperature near the wall is less for 25 lpm than 10 lpm sheath gas flow. At P5, the wall temperature is almost the same at both the sheath gas flow rates. The reason for these observations is that, with an increase in the sheath gas flow rate, higher

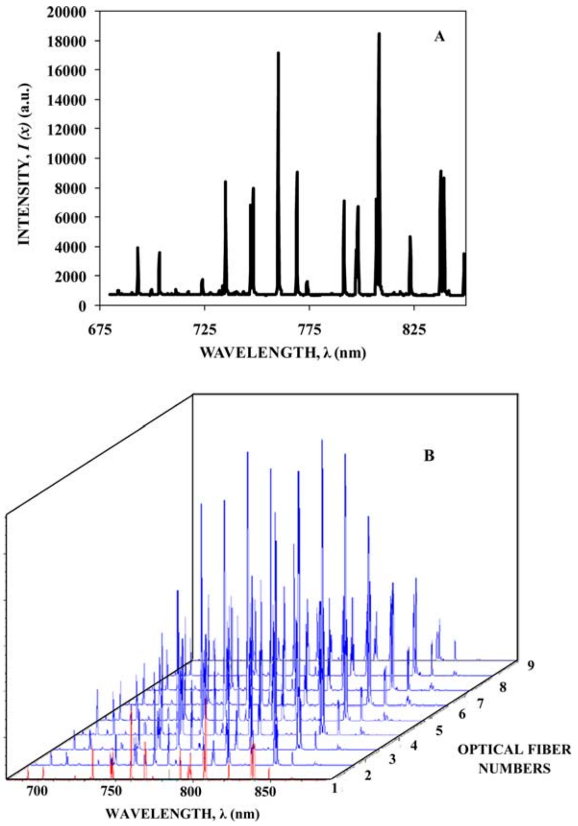

Figure 10. (A) A typical spectrum (680 to 890 nm) of Ar–I. (B) Spectral line intensities recorded through nine fibers for 4.73 kW RF power with 3 lpm plasma gas and 10 lpm sheath gas.

[Color figure can be viewed in the online issue, which is available at wileyonlinelibrary.com.]

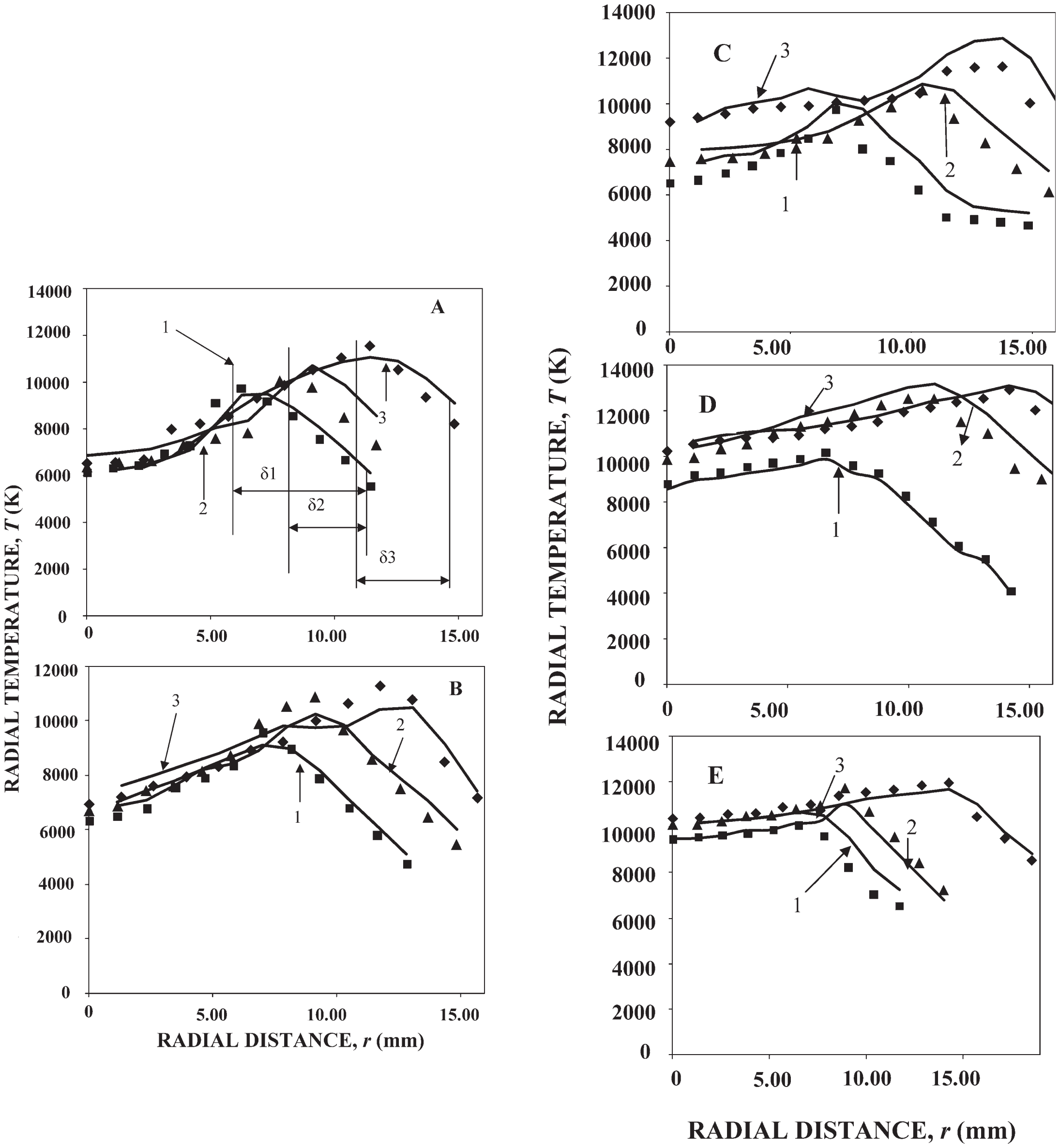

Figure 11. Radial temperature profiles at different axial locations with $Q_2 = 3$ lpm and $Q_3 = 10$ lpm and CFD predictions: axial locations: (A) $z = 153.1$ mm, (B) $z = 170.2$ mm, (C) $z = 192.2$ mm, (D) $z = 220.4$ mm, and (E) $z = 240.8$ mm; Present CFD predictions: (1) 4.73 kW; (2) 8.84 kW; and (3) 13.35 kW RF-power; Present in-house experimental points: ■4.73 kW; ▲8.84 kW; ◆ 13.35 kW RF-power.

amount of energy is taken away by the sheath gas and the region of diffusion of sheath gas into plasma region is bigger. Both these conditions would cause a decrease in the peak temperatures and a decrease in the skin depth. However, the important finding is that this argument is not true for all the axial positions considered in the present investigation. This is because a large vortex is created at high sheath gas flow rate, which leads to an increase in the temperature in the upstream region above the coil. This particular behavior of radial temperature with variation of sheath gas flow rate has not been reported so far in the published literature. Further, Figures 12A–E show the comparison between the

Table 6. Skin Depth Values at Various Axial Locations for Different Power Inputs and Sheath Gas Flow Rates

Sheath Gas Flow Rate	$Q_3 = 10$ lpm			$Q_3 = 25$ lpm		
Power input	4.73 kW	8.84 kW	13.35 kW	5.24 kW	9.26 kW	13.74 kW
Axial positions	Skin Depth (mm)					
P1	5.17	4.00	3.5	5.57	5.0	4.68
P2	5.75	5.65	3.89	6.6	5.16	3.23
P3	6.85	5.77	5.24	6.84	6.49	5.72
P4	6.6	5.46	4.38	6.63	5.13	3.50
P5	5.25	5.0	4.23	5.2	4.9	4.6

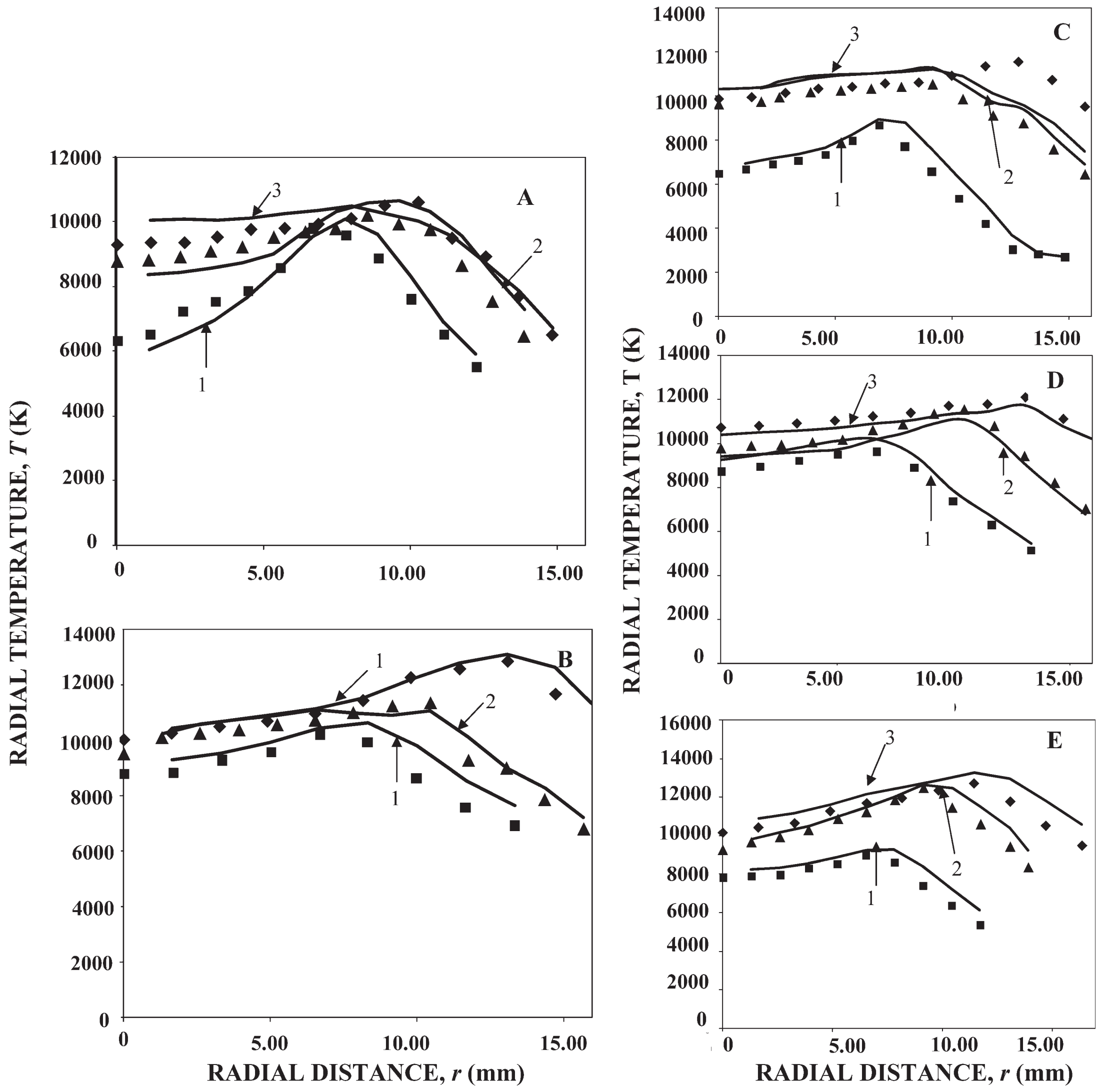

Figure 12. Radial temperature profile at various axial locations with Q_2: 3 lpm and Q_3: 25 lpm.

Present CFD predictions: (1) 5.24 kW; (2) 9.26 kW; and (3) 13.74 kW RF-power; Present in-house experimental points: ■5.24kW; ▲2. 9.26 kW; ◆ 13.74 kW RF-power; Axial locations:(A) $z = 153.1$ mm; (B) $z = 170.2$ mm; (C) $z = 192.2$ mm; (D) $z = 220.4$ mm; and (E) $z = 240.8$ mm.

CFD predictions and the experimental measurements for higher sheath gas flow rate of 25 lpm. For axial location P1, the agreement can be seen within 6% and 4% for the power inputs of 5.24 and 9.26 kW, respectively. Further, the agreement is within 8% for power input of 13.74 kW. For axial location P3, the agreement within 8% and 9% can be observed for power inputs of 9.26 and 13.74 kW, respectively. In addition, for axial locations P4 and P5 (Figures 12D, E) the agreement was found to be excellent and within 5%.

Axial Temperature Profiles. Axial temperature profile for 3 lpm plasma gas flow rate and 10 lpm sheath gas flow rate is shown in Figure 13A. Figure 13B shows the results for 3 lpm plasma gas flow and 25 lpm sheath gas flow. These figures show a sharp rise in temperature above the coil for the high sheath gas flow. The comparison between CFD predictions and experimental measurements can also be observed in Figures 13A and B. For sheath gas flow rate of 10 lpm, the axial temperatures predicted by CFD simulations show agreement within 5% for lower power ($P = 4.73$ and 8.84 kW, respectively), while for $P = 13.35$, the agreement is within 8%. For higher sheath gas flow rate of 25 lpm, similar good agreement can be observed.

Photographs of plasma for 10, 25, and 30 lpm sheath gas flow (Figure 14) show that the plasma region extends toward upstream locations with an increase in the sheath gas flow. This is corroborated with the axial temperature profile as shown in Figures 13A and B. To find the reason for the aforementioned observations, we resorted to the CFD simulation (discussed in Results and Discussion section) for the flow field in the ICP. The streamlines obtained from the CFD simulation are shown in Figure 15. It can be observed that for 10 lpm sheath gas flow, there is a vortex created in the coil region itself and hot gas is recirculated in this region. This does not lead to an increase in the temperature at the upstream locations above the coil region. For 25 lpm sheath gas, flow contour shows the existence of a single vortex and the hot plasma in the coil region can be seen to shift in the upstream direction. This is due to pressure gradient created by high sheath gas flow rate. As the hot gases flow upward, the temperature in this region increases and the plasma is seen above the coil as shown in the photographs

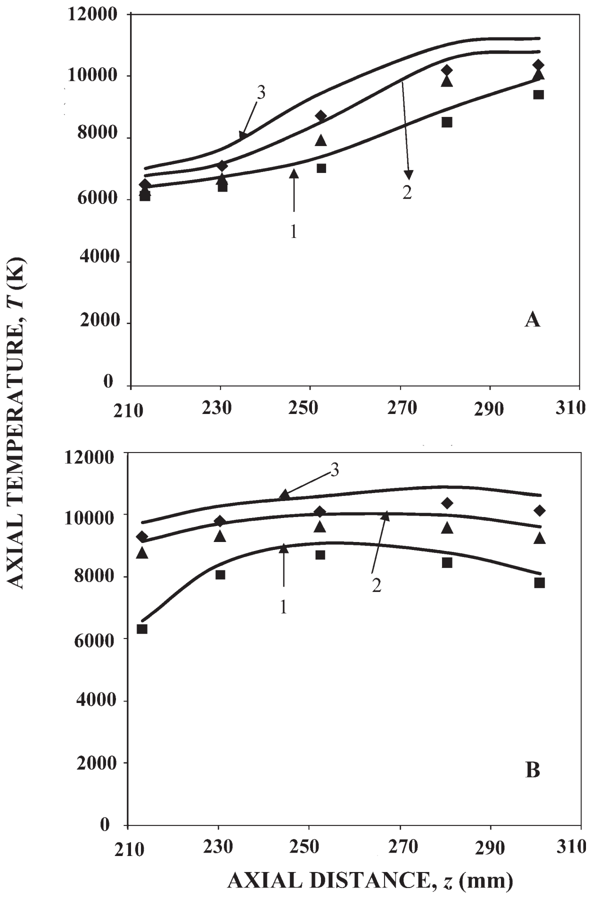

Figure 13. Axial temperature profile for constant Q_2 (3 lpm) while varying sheath gas flow (A) $Q_3 = 10$ lpm; Present CFD predictions: (1) 4.73 kW; (2) 8.84 kW; and (3) 13.35 kW RF-power. Present in-house experimental points: ■ 4.73 kW; ▲ 8.84 kW; ◆ 13.35 kW RF-power. (B) $Q_3 = 25$ lpm. Present CFD predictions: (1) 5.24 kW; (2) 9.26 kW; and (3) 13.74 kW RF-power; Present in-house experimental points: ■ 5.24kW; ▲ 9.26 kW; ◆ 13.74 kW RF-power.

(Figure 14). The observation of vortex is further explained as follows: at the inlet, the inflow of the sheath gas enters at very high velocities (typically 23.6–59 m/s), the corresponding Reynolds numbers being 21,500 and 54,000, respectively. The associated kinetic energy with the jet is responsible for the creation of vortices. It may be pointed out that the plasma gas velocity is about eight times lower than the sheath gas velocity. Therefore, the plasma gas has marginal influence on the vortex flow generated by the sheath gas (Figure 15). Further, the flow pattern of Figure 15 agrees with the flow patterns reported by Mostaghimi and Boulos.[22]

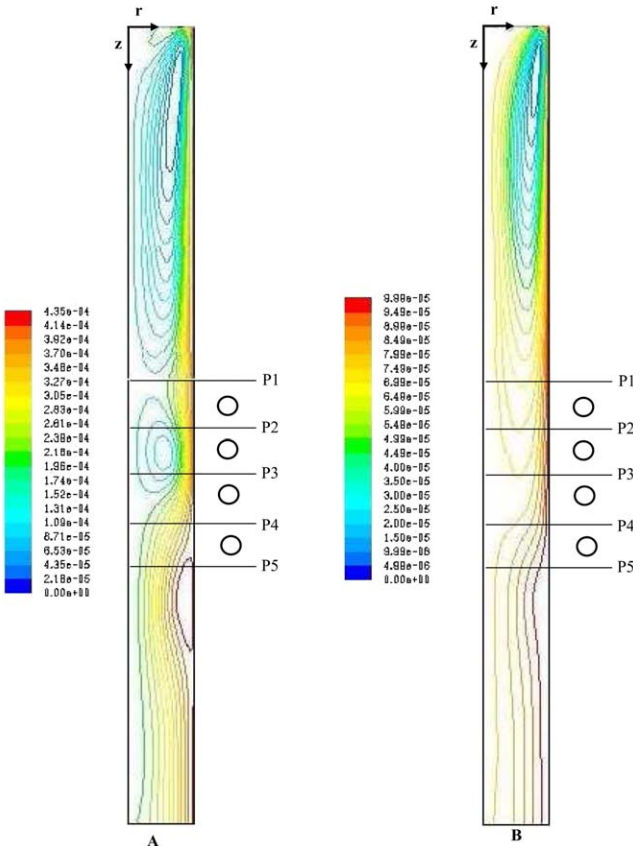

Figure 15. Flow fields of ICP torch operated at 5 kW RF power and 3 lpm plasma gas flow.

Streamlines for sheath gas flow rates (A) 10 lpm and (B) 25 lpm. [Color figure can be viewed in the online issue, which is available at wileyonlinelibrary.com.]

Turbulence Characteristics. The flows considered are highly turbulent as depicted by the Reynolds numbers (21,500–54,000; $\mathrm{Re} = Du_{\mathrm{sw}}\rho/\mu$; where D = diameter through which sheath gas flows; u_{sw} is the swirl velocity; ρ is the density; and μ is the viscosity). For the case of complex flow in plasma reactors, the Reynolds number may not indicate the quality of turbulence. Hence, we also investigate turbulent viscosity ratio and turbulent kinetic energy to understand the turbulence. Figure 16 shows the turbulent viscosity ratio and the turbulent kinetic energy in axial

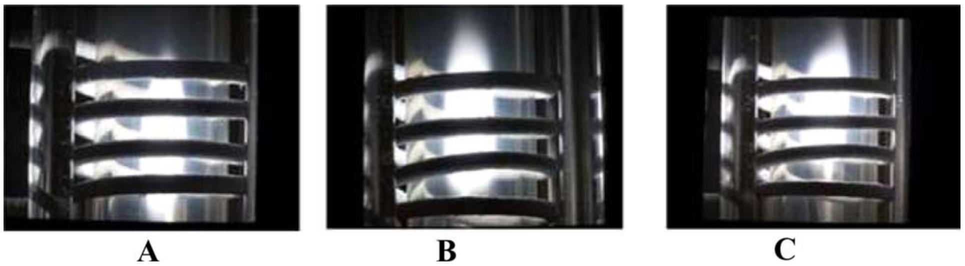

Figure 14. Photographs of plasma for sheath gas flow rates (A) 10 lpm, (B) 25 lpm, and (C) 30 lpm.

Plasma gas flow rate and DC power were held constant at 3 lpm and 3.75 kW, respectively. [Color figure can be viewed in the online issue, which is available at wileyonlinelibrary.com.]

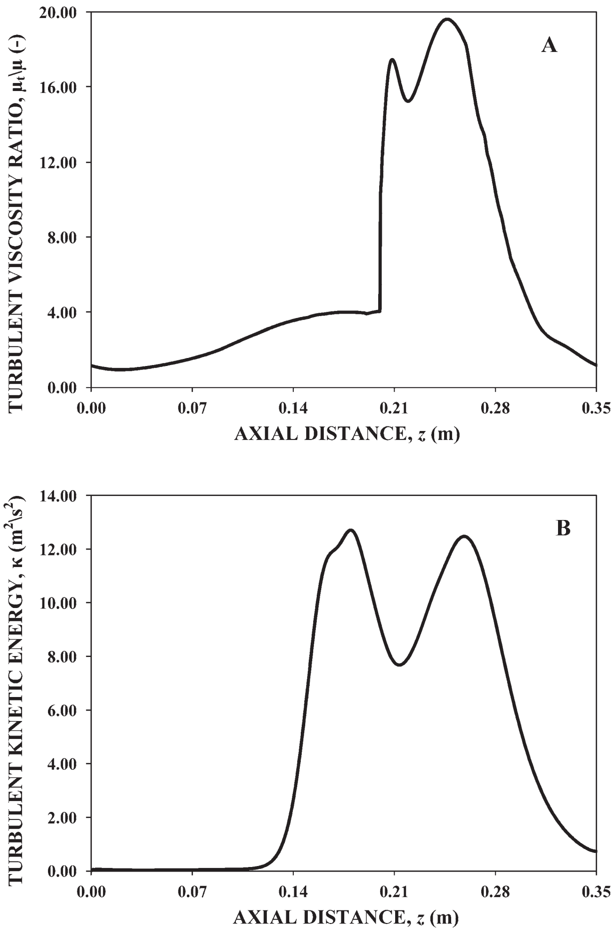

Figure 16. Axial variation of turbulent viscosity ratio and turbulent kinetic energy for $Q_2 = 3$ lpm and $Q_3 = 25$ lpm; $P = 7.5$ kW.

direction. The profiles suggest that the turbulent viscosity ratio is higher in regions near the coil (∼15) and lowers as we go away from the coil suggesting that there is high turbulence in the coil region. The turbulent kinetic energy also shows a similar trend thus showing the importance of the turbulence model.

Conclusion

1. The spatial distributions of temperature in an ICP torch working at atmospheric pressure have been measured. The radial temperature profiles were determined at different axial locations, at different sheath gas flow rates and over a wide range of power inputs. It was observed that the maximum temperature increases with an increase in the power input. As the power increases, the maximum temperature peak shifts toward the wall.
2. With an increase in the sheath gas flow, the plasma was found to move above the coil region. Further, the temperature at the axis was found to increase with an increase in the sheath gas flow rate. However, vice versa was observed on the downstream side of the coil especially at high power inputs. The trend of increase of maximum temperature with an increase in the power input was observed at higher sheath flow rates as well.
3. The axial temperature profiles show that the plasma volume reduces as the sheath gas flow rate increases and the axial temperature increases steeply.
4. The flow and the temperature fields have been simulated with CFD. The model predictions of the temperature and velocity profiles have been compared with various models and experimental data from the literature. A good agreement between the CFD predictions and the experimental measurements has been observed.
5. The CFD model was also applied to the present experimental geometry and the agreement between the model predictions and the experimental data was found to be very good within 5% at many locations and within 8% at all the locations.
6. The turbulent viscosity ratio is very high in the coil region with peak where turbulent viscosity is 18 times molecular viscosity. Similarly, the turbulent kinetic energy is also higher in the coil region. The work is in progress to characterize the quality of turbulence.[44,45]

Acknowledgments

The authors are thankful to Dr. L.M. Gantayet, Director, Beam technology development group, for his support during the course of this work. This work was made possible through continuing research grants from BRNS. The authors are thankful to Dr. D.S. Patil for upgrading the system to higher power and making the experimental system available to us. The authors are also thankful to Mr. P.K Soni, Mr. D.P. Chopade, Mr. S.T.Thakur, and Mr. D. K. Baskey for their technical support. The fellowship given by BRNS to SBP during the course of this work is gratefully acknowledged.

Notation

A_{I} = Imaginary part of vector potential
A_{R} = Real part of vector potential
$A_{\mathrm{R},p}$ = Real part of vector potential for *p*th volume as in Eq. 14
$A_{\mathrm{I},p}$ = Real part of vector potential for *p*th volume as in Eq. 13
A_θ = Vector potential in azimuthal direction
A_{ul} = Transition probability between the upper level u and the lower level l
B = Constant
C_{p} = Specific heat at constant pressure
C_μ = turbulence model constant
C_1 = turbulence model constant
C_2 = turbulence model constant
c = velocity of light as in Eq. 3
D = diameter through which sheath gas flows for calculation of Reynolds number
d_{c} = Coil tube diameter
E_{u} = Excitation energy of the upper level u
E_θ = Electric field in azimuthal direction
E_θ^* = Complex conjugate of electric field in azimuthal direction
$E(k')$ = Complete elliptic integrals
F_r = Radial body force
F_z = Axial body force
f = Oscillator frequency
G_κ = Production of turbulent kinetic energy
$G(k')$ = Function of complete elliptical integrals
$G(k'_p)$ = Function of complete elliptical integrals at *p*th volume
g_{l} = Statistical weight of lower level l
g_{u} = Statistical weight of upper level u
H = Enthalpy
H_1 = Height from upper flange to first coil winding
H_2 = Height from lowermost wall of coil winding to the torch bottom
H_{C} = Total height of the coil windings
H_{T} = Height of the 2-D axisymmetric domain considered for simulations

H_r = Radial component of magnetic field
H_z = Axial component of magnetic field
H_z^* = complex conjugate of axial component of magnetic field
h = Planck constant
I = Coil current
I_{ul} = Intensity of the atomic emission line
$I(r, \lambda)$ = Radial Intensity profile
I = (x) Intensity
i = imaginary as in Table 5, $(i = \sqrt{-1})$
K = Complete elliptic integrals
$K(k')$ = Complete elliptic integrals
k = Boltzmann constant as used in Eq. 2
k' = constant depending on radial and axial co-ordinates Eqs. 13, 14, 15, 16
k'_i = constant as in Eq. 16 for *i*th volume
k'_p = constant as in Eq. 16 for *p*th volume
κ = Turbulent kinetic energy as in Table 5
L = Optical path length
L_{C} = Length of the coil
L_{T} = Length of the 2-D axisymmetric domain considered for simulations used by Mostaghimi et al.[22]
n_{l} = Population density of lower level l
n_{u} = Population density of atoms excited to the upper energy level.
P = Input power
P_{c} = Distance of first coil winding from inlet as in Figure 4
P_{i} = locations at which temperature was measured.
p = pressure
Q_0 = total gas flow rate
Q_1 = central injection gas flow rate
Q_2 = plasma gas flow rate
Q_3 = sheath gas flow rate
R_0 = Radius of the confinement tube
R_{C} = Radius of the coil
R_i = Radius of *i*th coil
R_1 = Radius of outer quartz tube
r = Distance in radial direction
r_1 = Inner radius of injection tube
r_2 = Outer radius of injection tube
r_3 = Radius of intermediate tube
r_4 = Radius of intermediate tube
r_p = Radius of the *p*th control volume
S_p = Cross-section of the *p*th control volume
S = averaged strain term used in production term as in table 5
S_{ij} = Strain term as in Table 5
$|S|$ = Absolute value of averaged strain term used in production term as in table 5
$|S_{ij}|$ = Absolute value of strain term as in Table 5
T = Temperature
T_{kin} = (kinetic temperature) corresponds to translational motion of particles.
T_{exe} = (excitation temperature) which shows how the electronic excited states are distributed
T_{ion} = (ion temperature) which shows translational temperature of ions.
T_{e} = (electron temperature) is translational temperature of electrons.
T_{nu} = (neutral atom temperature) is translational temperature of neutral atoms
T_{rot} = (rotational temperature) which is a measure of how rotational levels of molecules or radicals are distributed.
T_{s} = Inside surface temperature of quartz tube
T_{w} = External (wall) surface temperature of quartz tube (300 K)
U_{p} = local energy dissipation rate
U_{R} = Volumetric radiation heat losses
u_r = Radial component of velocity
u_θ = Tangential (swirl) component of velocity
$u_{\theta 2}$ = Tangential (swirl) component of velocity for a particular radius range as in Eq. 6
$u_{\theta 3}$ = Tangential (swirl) component of velocity for a particular radius range as in Eq. 6
u_z = Axial component of velocity
z = Distance in axial direction
z_p = Height of the boundary at *p*th control volume.
z_i = Height of the *i*th coil

Greek symbols

α_{eff} = Thermal diffusivity
δ_{w} = Tube wall thickness as in Figure 4
δ = Skin depth
δ_1 = Skin depth at power 4.73 kW
δ_2 = Skin depth at power 8.84 kW
δ_3 = Skin depth at power 13.35 kW
ε = Turbulent Energy dissipation rate
λ_{ul} = Wavelength of transition from upper level u and lower level l
λ = Thermal conductivity
λ_{w} = Thermal conductivity of the quartz confinement tube (λ_{w}= 1.047 W/mK)
$\mu_t{}^t$ = Turbulent viscosity
μ_0 = Permeability of free space
ω = Angular frequency
ρ = Density
μ = kinematic viscosity
v = dynamic viscosity
v_{ul} = Frequency of radiation
v_{t} = turbulent dynamic viscosity
σ = Electrical conductivity
σ_ε = constant in turbulence energy dissipation equation
σ_{k} = constant in turbulence kinetic energy dissipation equation
σ_p = Electrical conductivity at *p*th control volume
σ_t = turbulencePrandtl number

Subscript

i = location number
l = lower level
u = Upper level

Abbreviation

CFD = computational fluid dynamics
ICP = Inductively Coupled Plasma
LTE = Local Thermal Equilibrim

Literature Cited

1. Vurzel FB, Polak LS. Plasma chemical technology—the future of the chemical industry. *Ind Eng Chem.* 1970;62:88–22.
2. Chen MY, Johnson DL. Effects of additive gases on radio-frequency plasma sintering of alumina. *J Mater Sci.* 1992;27:191–196.
3. Bolous MI. The inductively coupled radio frequency plasma. *High Temp Mater Process.* 1997;1:17–39.
4. Shigeta M, Sato T, Nishiyama H. Numerical simulation of a potassium-seeded turbulent RF inductively coupled plasma with particles. *Thin Solid Films.* 2003;435:5–12.
5. Liao Y, Wong K, McVittie JP, Saraswat KC. Abatement of perfluorocarbons with an inductively coupled plasma reactor. *J Vac Sci Technol.* 1999;205:22–29.
6. Guddeti, RR, Knight RR, Grossmann ED. Depolymerization of polypropylene in an induction-coupled plasma (ICP) reactor. *Ind Eng Chem Res.* 2000;39:1171–1176.
7. Mohai I, Szèpvölgyi J, Károly Z, Mohai M, Tóth M, Babievskaya IZ, Krenev VA. Reduction of metallurgical wastes in an RF thermal plasma reactor. *Plasma Chem Plasma Process.* 2001;21:547–563.
8. Bretagnol F, Tatoulian M, Arefi-Khonsari F, Lorang G, Amouroux J. Surface modification of polyethylene powder by nitrogen and ammonia low pressure plasma in a fluidized bed reactor. *React Funct Polym.* 2004;61:221–232.
9. Ye R, Murphy AB, Ishigaki T. Numerical modeling of an Ar–H2 radio-frequency plasma reactor under thermal and chemical nonequilibrium conditions. *Plasma Chem Plasma Process.* 2007;27:189–204.
10. Abanades S, Tescari S, Rodat S, Flamant G. Natural gas pyrolysis in double-walled reactor tubes using thermal plasma or concentrated solar radiation as external heating source. *J Nat Gas Chem.* 2009;18:1–8.
11. Jia L, Gitzhofer F. Nano-particle sizing in a thermal plasma synthesis reactor. *Plasma Chem Plasma Process.* 2009;29:497–513.
12. Blanchard J, Abatzoglou N, Eslahpazir-Esfandabadi R, Gitzhofer F. Fischer-Tropsch synthesis in a slurry reactor using a nanoiron carbide catalyst produced by a plasma spray technique. *Ind Eng Chem Res.* 2010;49:6948–6955.
13. Hody H, Pireaux JJ, Choquet P, Moreno-Couranjou M. Plasma functionalization of silicon carbide crystalline nanoparticles in a novel low pressure powder reactor. *Surf Coat Technol.* 2010;205:22–29.
14. Pristavita R, Mendoza-Gonzalez NY, Meunier JL, Berk D. Carbon blacks produced by thermal plasma: the influence of the reactor

geometry on the product morphology. *Plasma Chem Plasma Process.* 2010;30:267–279.
15. Kelliget JW, El-Kaddah N. The effect of coil design on material synthesis in an inductively coupled plasma torch. *J Appl Phys.* 1988; 64:2948–2954.
16. Kornblum GR, De Galan, L. Spatial distribution of the temperature and the number densities of electrons and atomic and ionic species in an inductively coupled RF argon plasma. *Spectrochim Acta.* 1977; 32B:71–96.
17. Barnes RM, Scheicher RG. Temperature and velocity distributions in an inductively coupled plasma. *Spectrochim Acta.* 1981;36B:81–101.
18. Joshi NK, Thiagarajan TK, Rohatgi VK, Ashtamoorthy TS. The spatial distribution of excitation temperature and electron density in an inductively coupled argon plasma. *J Phys D.* 1988;21:1121–1124.
19. Hughes DW, Wooding ER. The temperature distribution in an H-mode R.F. plasma torch. *Phys Lett.* 1967;24A:70–71.
20. Mostaghimi J, Proulx P, Boulos MI, Parametric study of flow and temperature fields in an inductively coupled RF Plasma Torch. *J Plasma Chem Plasma Process.* 1985;4:199–217.
21. Boulos MI. The inductively coupled R.F. (radio-frequency) plasma. *Pure Appl Chem.* 1985;57:1321–1352.
22. Mostaghimi J, Boulos MI. Two dimensional electromagnetic field effects in induction plasma modeling. *Plasma Chem Plasma Process.* 1989;9:25–44.
23. Nishiyama H, Muro Y, Kamiyama S. The control of gas temperature and velocity field of a RF induction thermal plasma by injecting secondary gas. *J Phys D: Appl Phys.* 1996;29:2634–2643.
24. Xue S, Proulx P, Boulos MI. Extended-field electromagnetic model for inductively coupled plasma. *J Phys D: Appl Phys.* 2001;34: 1897–1906.
25. Bernardi D, Colombo V, Ghedini E, Mentrelli A. Comparison of different techniques for FLUENT based treatment of electromagnetic field in inductively coupled plasma torches. *EurPhys J D.* 2003; 27:55–72.
26. Joshi NK, Sahasrabudhe SN, Sreekumar KP, Venkataramani N. Variation of axial temperature in thermal plasma jets. *Meas Sci Technol.* 1997;8:1146–1150.
27. Cremers CJ, Birkebak RC. Application of the Abel Integral equation to spectrographic data. *Appl Opt.* 1966;5:1057–1063.
28. Ignjatovic LM, Mihajlov AA. The realization of Abel's inversion in the case of discharge with undetermined radius. *J Quant Spectrosc Radiat Transfer.* 2002;72:677–689.
29. Benenson DM, Kwok HS. On plasma diagnostics. *Pure Appl Chem.* 1982;54:1157–1180.
30. Joshi JB, Ranade VV, Computational fluid dynamics for designing process equipment: expectations, current status and path forward. *Ind Eng Chem Res.* 2003;42:1115.
31. Ekambara K, Dhotre MT, Joshi JB, CFD simulations of bubble column reactors: 1D, 2D and 3D approach. *Chem Eng Sci.* 2005;60: 6733–6746.
32. Murthy B N, Joshi J B. Assessment of Standard k—ε, RSM and LES turbulence models in a baffled stirred vessel agitated by various impeller designs. *Chem Eng Sci.* 2008;63:5468.
33. Murthy BN, Ghadge RS, Joshi JB. CFD simulations of gas-liquid-solid stirred reactor: prediction of critical impeller speed for solid suspension. *Chem Eng Sci.* 2007;62:7184.
34. Reed TB. Induction-coupled plasma torch. *J Appl Phys.* 1961;32: 821–824.
35. Mostaghimi J, Proulx P, Boulos MI. A two temperature model of the inductively coupled rf plasma. *J Appl Phys.* 1987;61:1753–1760.
36. Johannes J, Bartel T, Hebner GA, Woodworth J, Economou GA, Economou DJ. Direct simulation Monte Carlo of inductively coupled plasma and comparison with experiments. *J Electrochem Soc.* 1997; 144:2448–2455.
37. Panagopoulos T, Kim D, Midha V, Economou DJ. Three dimensional simulation of inductively coupled plasma reactor. *J Appl Phys.* 2002;91:2687–2696.
38. Economou D J. Modeling and simulation of fast neutral beam sources for materials processing. *Plasma Process Polym.* 2009;6:308–319.
39. Saha MN. On a physical theory of stellar spectra. *Proc R Soc London Ser A.* 1921;99: 135–153.
40. Patankar SV. *Numerical Heat Transfer and Fluid Flow*. New York: McGraw-Hill, 1980.
41. Launder BE, Spalding DB. The numerical computation of turbulence flows. *Comput Methods Appl Eng.* 1974;3:269.
42. Lesinski J, Gagne R, Boulos MI. Gas and Particle Velocity Measurements in an Induction Plasma. In: *Proceedings of 5th International Symposium on Plasma Chemistry*. Edinburg, U.K. 1981.
43. Watanabe T, Yanase K, Honda T, Kanzawa A. The flow temperature and concentration fields in a radio-frequency argon-helium plasma. *J Chem Eng Jpn.* 1990; 23:389–395.
44. Kulkarni AA, Joshi JB, Ravi Kumar V, Kulkarni BD. Application of multi resolution analysis for simultaneous measurement of gas and liquid velocities and fractional gas hold-up in bubble columns using LDA. *Chem Eng Sci.* 2001;56:5037–5048.
45. Joshi JB, Tabib MV, Deshpande SS, Mathpati CS. Dynamics of flow structures and transport phenomena-I: experimental and numerical techniques for identification and energy content of flow structures. *Ind Eng Chem Res.* 2009;48:8244–8284.

Manuscript received Feb. 28, 2013, and revision received June 19, 2014.